

1 **North-south Asymmetric Nightside Distorted Transpolar Arcs within A Framework**  
2 **of Deformed Magnetosphere-Ionosphere Coupling: IMF- $B_y$  Dependence,**  
3 **Ionospheric Currents, and Magnetotail Reconnection**  
4

5 Motoharu Nowada<sup>1</sup>, Qiu-Gang Zong<sup>2</sup>, Benoît Hubert<sup>3</sup>, Quan-Qi Shi<sup>1</sup>, Yong-Fu Wang<sup>2</sup>,  
6 Jun Yang<sup>1</sup>, Adrian Grocott<sup>4</sup>, Alexander W. Degeling<sup>1</sup>, An-Min Tian<sup>1</sup>,  
7 Xu-Zhi Zhou<sup>2</sup>, and Chao Yue<sup>2</sup>

8 <sup>1</sup>Shandong Key Laboratory of Optical Astronomy and Solar-Terrestrial Environment, School of  
9 Space Science and Physics, Institute of Space Sciences, Shandong University, Weihai,  
10 Shandong, People's Republic of China.

11 <sup>2</sup>Institute of Space Physics and Applied Technology, School of Earth and Space Sciences, Peking  
12 University, People's Republic of China.

13 <sup>3</sup>Space science, Technologies and Astrophysics Research (STAR) Institute, Université de Liège,  
14 Belgium.

15 <sup>4</sup>Space and Planetary Physics Group, Department of Physics, Lancaster University, Lancaster,  
16 UK.

17  
18 Key points:

- 19 1. A new morphological type of transpolar arc, characterized by large nightside distortions in the  
20 pre- or post-midnight sector, is described.
- 21 2. Nightside reconnection and magnetotail deformation by IMF penetration play essential roles  
22 in the formation of nightside distorted TPA.
- 23 3. Nightside distorted TPAs can be used as a remote-sensing tool to diagnose globally IMF-  
24 deformed magnetospheric processes.

25  
26 Corresponding Authors:

27 Motoharu Nowada (moto.nowada@sdu.edu.cn),

28 Qiu-Gang Zong (qgzong@pku.edu.cn),

29 Quan-Qi Shi (sqq@sdu.edu.cn)

30 **Abstract**

31 The terrestrial magnetosphere is perpetually exposed to, and significantly deformed by the  
32 Interplanetary Magnetic Field (IMF) in the solar wind. This deformation is typically detected at  
33 discrete locations by space- and ground-based observations. Earth's aurora, on the other hand, is  
34 a globally distributed phenomenon that may be used to elucidate magnetospheric deformations  
35 caused by IMF variations, as well as plasma supply from the deformed magnetotail to the high-  
36 latitude atmosphere. We report the utilization of an auroral form known as the transpolar arc  
37 (TPA) to diagnose the plasma dynamics of the globally deformed magnetosphere. Nine TPAs  
38 examined in this study have two types of a newly identified morphology, which are designated as  
39 "J"- and "L"-shaped TPAs from their shapes, and are shown to have antisymmetric  
40 morphologies in the Northern and Southern Hemispheres, depending on the IMF polarity. The  
41 TPA-associated ionospheric current profiles suggest that electric currents flowing along the  
42 magnetic field lines (Field-Aligned Currents: FACs), connecting the magnetotail and the  
43 ionosphere, may be related to the "J"- and "L"-shaped TPA formations. The FACs can be  
44 generated by velocity shear between fast plasma flows associated with nightside magnetic  
45 reconnection and slower background magnetotail plasma flows. Complex large-scale TPA FAC  
46 structures, previously unravelled by an Magnetohydrodynamic (MHD) simulation, cannot be  
47 elucidated by our observations. However, our interpretation of TPA features in a global context  
48 facilitates the usage of TPA as a diagnostic tool to effectively remote-sense globally deformed  
49 terrestrial and planetary magnetospheric processes in response to the IMF and solar wind plasma  
50 conditions.

51

52 Keywords: Nightside Distorted Transpolar Arc; Solar Wind-Magnetotail-  
53 Ionosphere/Atmosphere Coupling; Magnetospheric Diagnosis; Magnetotail Magnetic  
54 Reconnection; Plasma Flow Shear; Field-Aligned Currents

55 **Plain Language Summary**

56 In magnetospheric physics, the aurora is one of the most important phenomena in qualitatively  
57 and quantitatively understanding the transfer of plasma and energy from the solar wind to the  
58 high-latitude atmosphere via terrestrial and other planetary magnetospheres. To understand the  
59 global picture of the plasma supply from the terrestrial magnetosphere, deformed by the  
60 Interplanetary Magnetic Field (IMF) in the solar wind, to the auroral zone, the formation process  
61 of a new morphology of auroral transpolar arc (TPA) is investigated in this study. The source of  
62 these TPAs can be the electric currents flowing along magnetic field lines, induced by the plasma  
63 flows in the magnetosphere. The conventional TPA has a straight bar shape, which connects the  
64 nightside and dayside of the auroral oval. The new TPA morphologies, on the other hand, have  
65 significant “distortions” toward pre- and post-midnight at their nightside ends, which may be  
66 caused by magnetic field line twisting and magnetosphere deformations due to the action of the  
67 IMF. Our results facilitate a paradigm shift in understanding the implications of TPA structure  
68 on global scale dynamics in the deformed magnetosphere, and as such, the usage of the auroral  
69 TPA shape as a tool to diagnose global-scale magnetospheric effects.

## 70 **1. Introduction**

71 The terrestrial magnetosphere, which dynamically changes through interactions with the high-  
72 speed plasma streams and Interplanetary Magnetic Field (IMF) originating from the Sun,  
73 effectively shields life on Earth from harmful radiation effects associated with these particles  
74 (Black, 1967; Glassmeier et al. 2009, 2010; Shi et al. 2013). The geomagnetic field surrounding  
75 the Earth also plays a role in preventing the atmosphere from escaping into space (Wei et al.  
76 2014). Therefore, it is important to understand the morphologies and dynamics of our terrestrial  
77 magnetosphere, in particular, the processes by which plasma is supplied to, and released from,  
78 the magnetotail and transferred to the high-latitude atmosphere or ionosphere.

79 Significant global magnetospheric effects are produced not only by changes in the IMF north-  
80 south component (IMF- $B_z$ ) but also its dawn-dusk component (IMF- $B_y$ ). A series of  
81 observational studies (Kaymaz et al. 1995; Nishida et al. 1995, 1998; Pitkänen et al. 2013, 2015,  
82 2017) have found that under dominant IMF- $B_y$  conditions, the magnetotail (plasma sheet)  
83 becomes increasingly twisted with down-tail distance, caused by the penetration of IMF- $B_y$  into  
84 the magnetotail. Magnetotail deformation and IMF penetration to the magnetotail have been  
85 attributed to magnetic reconnection under dominant IMF- $B_y$  conditions (Gosling et al. 1990;  
86 Cowley, 1981, 1994; Grocott et al., 2007; Tenfjord et al. 2015, 2018), which causes asymmetries  
87 in the magnetosphere. Inside the deformed magnetosphere, magnetic reconnection can occur and  
88 release energized plasma (electrons) earthward and tailward (Petrukovich et al. 1998; Nagai et al.  
89 2001; Angelopoulos et al. 2013; Wang et al. 2020, and references therein). The “source” of  
90 auroral arcs, which are frequently seen within the polar cap region (sun-aligned arcs), is  
91 considered to be the currents flowing along the magnetic field, carried by precipitating energetic  
92 plasma (electrons) (see the details in a review by Zhu et al. 1997). These field-aligned electron  
93 flows originate from the magnetotail. When magnetic reconnection occurs in the nightside  
94 magnetosphere, magnetic energy stored in the magnetotail is converted to particle kinetic energy,  
95 producing accelerated plasma flows out of the reconnection region as earthward and distant-  
96 tailward high-speed exhaust jets (e.g., Baumjohann et al. 1989, 1990; Angelopoulos et al. 1992,  
97 1994). As a result, localized fast plasma flows associated with reconnection are conveyed along  
98 the field lines, and embedded within lower velocity plasma flows of magnetospheric origin in the  
99 magnetotail. Flow shear across field lines between high and low velocity flow regions generates

100 electric currents that flow parallel to magnetic field lines, known as Field-Aligned Currents  
101 (FACs) (Hasegawa and Sato, 1979; Birn and Hesse, 1991; Fairfield et al. 1999). Evidence of this  
102 process has been compiled by sparse, spatially discrete ground-based, and space-based magnetic  
103 field and particle observations (Angelopoulos et al. 1996; Fairfield et al. 1999, and references  
104 therein). However, the aurorae seen in the Northern and Southern Hemispheres can be used as a  
105 tool to globally diagnose these magnetospheric processes.

106 A specific auroral form observed under northward IMF- $B_z$  conditions, the Transpolar arc  
107 (TPA), occurs at extremely high latitudes. This is identified as a “bar-shaped” emission within  
108 the polar cap region, extending from the poleward edge of the nightside auroral oval toward the  
109 dayside (Frank et al. 1982). Its formation mechanism and features have been explained in terms  
110 of magnetospheric convection and its relationship with the IMF orientation (Fear and Milan,  
111 2012a, 2012b). TPA locations depend on the extent of clockwise or counter-clockwise plasma  
112 sheet twisting (viewed from the magnetotail), which is controlled by the IMF- $B_y$  polarity (i.e.  
113 either dawnward or duskward, for clockwise or counter-clockwise twisting) (Tsyganenko and  
114 Fairfield, 2004; Tsyganenko and Stenov, 2005; Tsyganenko et al. 2015; Cumnock et al. 2002).

115 The TPA formation model proposed by Milan et al. (2005) is one of the most representative  
116 TPA formation models based on nightside magnetic reconnection, and has been applied to  
117 explain the developments of many TPAs (Fear and Milan, 2012a, b; Kullen et al. 2005; Nowada  
118 et al. 2018). In this model, the TPA growth is attributed to the continual formation of newly  
119 closed field lines by magnetotail reconnection, whose location retreats tailward. Several “non-  
120 straight” TPAs were also identified in previous statistical studies (Fear and Milan, 2012a; Kullen  
121 et al., 2015), which contrast with the “bar”-shaped TPA (hereafter, referred to as a “regular  
122 TPA”) previously discussed (Fear and Milan, 2012a, b; Kullen et al. 2005; Nowada et al. 2018).  
123 However, neither the physical mechanism for these TPAs, nor their implications on the IMF-  
124 deformed magnetospheric dynamics have been discussed.

125 In this paper, we first identify a new morphological type of nightside distorted TPA, which is  
126 distinct from the “regular” TPA. Utilizing space-borne images and in-situ magnetotail  
127 observations, together with ground-based geomagnetic field and high-frequency (HF) radar  
128 observations, we obtain a global picture of the plasma supply from the deformed magnetotail to  
129 the high-latitude atmosphere (auroral zone) by considering the implications of these observations

130 in the nightside distorted TPA formation. In so doing, we demonstrate that the nightside distorted  
131 TPAs can be used as a remote-sensing diagnostic tool for global magnetospheric effects.

132

## 133 **2. Instrumentation**

134 New morphological TPAs discussed in this paper were identified using a large database  
135 spanning 5 years of auroral observations from 2000 to 2005 by the Wideband Imaging Camera  
136 (WIC), which is part of the Far Ultraviolet (FUV) instrument (Mende et al. 2000a, b, c) onboard  
137 Imager for Magnetopause-to-Aurora Global Exploration (IMAGE) , launched in March, 2000.  
138 IMAGE FUV-WIC imaged the aurora in a broad wavelength range from 140 nm to 190 nm, with  
139 a cadence of 2 minutes. From this database, we chose 9 nightside distorted TPAs based on visual  
140 inspection, which were clearly imaged in the plots of the IMAGE FUV-WIC data after the  
141 removal of dayglow and background contamination, as described below.

142 The IMAGE FUV-WIC data frequently includes optical contamination, such as sunlight  
143 (dayglow) and instrumental optical noise. These non-auroral signals are removed as much as  
144 possible from the original WIC images by least squares fitting techniques. The image is  
145 separated into two parts along the terminator, but still has an overlap between the dayside and the  
146 nightside parts (i.e. the nightside part extends somewhat over the dayside and vice versa). The  
147 dayside part of the image is fitted using a two-dimensional Fourier series while the nightside part  
148 is fitted using a two-dimensional polynomial. The auroral emission is excluded from the fitting  
149 process, and the overlap region is used to produce a smooth merging of both parts. The fitted  
150 glow and background are interpolated over the auroral region (including over the transpolar arc  
151 region, which is excluded from the fitting process as well). Subtraction of the fitted signal from  
152 the images taken and observed over the whole Earth extracts only the auroral signals, albeit with  
153 some unavoidable noise contamination. The light from stars, which occasionally appear over the  
154 limb of the Earth, can be somewhat scattered and leave their traces on the images. Note that  
155 these optical effects are hard to remove, and must not be confused with a real emission from the  
156 upper atmosphere. Because non-auroral signals generated by the bright dayglow can only  
157 approximately be represented by this method, the optical contamination cannot be completely  
158 cleaned from the image. In this study, we discuss the characteristics of unique TPA  
159 morphologies, identified based on significant auroral signals, which were extracted through these

160 IMAGE FUV-WIC data processing.

161

### 162 **3. Results**

#### 163 **3.1 Overview of Nightside Distorted TPAs**

164 “Regular” TPAs generally have a straight shape connecting the nightside and dayside auroral  
165 oval. In contrast, all TPAs discussed in this paper have a significant “distortion” at the nightside  
166 ends (hereafter, referred to as “nightside distorted TPAs”). Figure 1 shows false color images of  
167 8 representative nightside distorted TPAs, which were identified from IMAGE-FUV-WIC  
168 observations. The top (bottom) row of panels correspond to cases of  $IMF-B_y < 0$  ( $IMF-B_y > 0$ ),  
169 and the first three columns show Northern Hemisphere (NH) observations, while the last column  
170 displays Southern Hemisphere (SH) observations. Each panel is oriented such that the top, right,  
171 bottom and left sides, corresponding to noon (12 MLT), dawn (6 MLT), midnight (24 MLT), and  
172 dusk (18 MLT), respectively. The color scale is expressed in Analogic-Digital Units (ADU),  
173 which is proportional to the observed auroral brightness (Mende et al. 2000b). The upper panels  
174 (a) to (c) display dawnside TPAs with the nightside ends distorted toward midnight or pre-  
175 midnight, observed in the NH. Hereafter, we identify these as “J”-shaped TPAs based on their  
176 resemblance to the letter “J”. In all observed TPAs, the “J”-shaped TPAs in the NH occur during  
177 a negative (dawnward)  $IMF-B_y$  interval. The bottom panels (e) to (g) show nightside distorted  
178 TPAs with the opposite chirality that occurred on the duskside, in which the nightside ends get  
179 distorted toward midnight or post-midnight. We identify these as “L”-shaped TPAs based on  
180 their resemblance to the letter “L”. Panels (d) and (h) show observations in the SH during  
181 negative and positive  $IMF-B_y$  intervals, respectively. Interestingly, these two panels appear to  
182 show the opposite chirality to their NH counterparts under the same IMF conditions, with an  
183 “L”-shaped TPA (panel d), and a “J”-shaped TPA (panel h). The detailed growth of these  
184 representative four nightside distorted TPAs and corresponding solar wind conditions are shown  
185 in the Supporting Information (Figure S1).

186

#### 187 **3.2 In-situ Duskside Magnetotail Observations during the Nightside Distorted TPA interval**

188 All of the “J (L)”-shaped TPAs identified in our study, shown in Figure 1, originate in the

189 nightside main auroral oval and protrude toward the dayside, indicating that nightside magnetic  
190 reconnection plays a significant role in the formation of these TPAs (see the detailed series of  
191 figures shown in Figure S1). In-situ magnetotail observations were examined during the  
192 nightside distorted TPA intervals. Figure 2 shows a summary plot of the solar wind (observed by  
193 Advanced Composition Explorer: ACE), and the magnetotail (observed by Geotail) on March  
194 12<sup>th</sup>, 2002, when the “L”-shaped TPA was detected by IMAGE FUV-WIC. The panels from top  
195 to bottom show: the IMF- $B_y$  and  $-B_z$  components in GSM coordinates, the solar wind dynamic  
196 pressure, the Geotail measurements of the sun-earth (GSM-X), dawn-dusk (GSM-Y) and north-  
197 south (GSM-Z) magnetic field components in the duskside magnetotail, the associated magnetic  
198 field elevation angle, and the ion flow velocity in GSM and Mean Field Coordinates (MFC),  
199 which has axes parallel and perpendicular to local magnetic field lines over the 1 hour 40  
200 minutes time interval between 00:10 UT and 01:50 UT. During this interval, the “L”-shaped  
201 TPA intensifications were clearly identified from 00:31:34 UT to 00:58:12 UT and from  
202 01:10:29 UT to 01:37:07 UT, which are bracketed by two gold broken lines, and labelled ‘LS’.  
203 The GSM locations of Geotail when the “L”-shaped TPAs were seen are indicated below the last  
204 panel of Figure 2(a). The IMF- $B_y$  and  $-B_z$  components were oriented roughly duskward  
205 (positive) and northward (positive) during both TPA intervals. Associated solar wind dynamic  
206 pressure showed no significant changes. The large abrupt decreases and increases twice seen in  
207 the Geotail- $B_x$  component indicate multiple crossings (four times) of the magnetotail current  
208 sheet from the Northern to Southern, and from the Southern to Northern Hemispheres,  
209 respectively. The variations of associated  $B_y$  and  $B_z$  components were anti-correlated with that of  
210 the  $B_x$  component. Particular enhancements of the  $B_z$  component and elevation angle, seen in  
211 both LS intervals, suggest that the nightside magnetospheric configuration becomes more  
212 “dipole-like”, presumably resulting from a pile-up of the magnetic flux transported from the  
213 distant magnetotail. Before the  $B_z$  enhancements, the  $V_x$  component shows earthward “bursty”  
214 enhancements, indicating the occurrence of magnetotail magnetic reconnection at the onset and  
215 the initial stage of the two “L”-shaped TPAs. Taking a look at the x-directional components of  
216 plasma flow speed parallel and perpendicular to the field lines ( $V_{\text{parax}}$ ,  $V_{\text{perpx}}$ ), this flow burst had  
217 a much more dominant field-aligned component ( $V_{\text{parax}}$ ) than the perpendicular flow velocity  
218 ( $V_{\text{perpx}}$ ). The second flow bursts seen during the second LS interval also had a strong field-  
219 aligned velocity. These earthward flow burst profiles also suggest the tailward retreat of the



220 reconnection locations; the  $V_x$  component in the first interval had already started to decrease at  
221 the onset of the “L”-shaped TPA, and the flow burst velocity during the second “L”-shaped TPA  
222 interval was lower than that in first TPA interval (considering that there was little difference in  
223 the satellite positions between first and second TPA intervals). The  $V_z$  components at the two  
224 earthward flow bursts were negative, suggesting that the plasma in the lobe region was flowing  
225 into the reconnection region in the plasma sheet. Further energized plasma was associated with  
226 the fast plasma flows because the temperature abruptly enhanced at the time of the first flow  
227 burst, however, a significant temperature enhancement was not seen at the second fast flow event.  
228 The magnetic pressure ( $B_t^2/2\mu_0$ ;  $B_t$  is the magnetic field intensity) was higher than the plasma  
229 pressure ( $N_i k T_i$ ) during the two flow burst intervals, indicating that the regions where the two  
230 flow burst events occurred may be plasma sheet boundary layer (PSBL). Before the fast flow  
231 burst, Geotail was situated in the lobe region in the Northern Hemisphere, but detected the fast  
232 plasma flow just after its entry to the PSBL. This is because the plasma pressure began to  
233 gradually enhance against a slight decrease of the magnetic pressure. After the flow burst, the  
234 plasma pressure was higher than the magnetic pressure due to the migration of Geotail to the  
235 inner plasma sheet (central plasma sheet). The satellite experienced multiple crossings of the  
236 current sheet. During the second LS interval, Geotail transiently went out of the plasma sheet,  
237 and recorded a weaker second flow burst in the PSBL. After the detection of the second flow  
238 burst, the satellite returned to the inner plasma sheet. Baumjohann et al. (1988) reported that  
239 faster plasma flows in the PSBL tend to have dominant field-aligned components, that is, away  
240 from the magnetic equatorial plane, which is consistent with our interpretation in which the two  
241 flow bursts seen here occurred in the PSBL. Furthermore, these fast plasma flows seem not to be  
242 associated with a “plasma bubble” (Chen and Wolf, 1993). If “plasma bubble” structures were  
243 formed by magnetotail reconnection and resultant fast plasma flows were driven, the plasma  
244 flows should have flow velocity components dominantly perpendicular to the magnetic field  
245 lines (see figure 3 in Chen and Wolf, 1993). Chen and Wolf (1993) also pointed out that when  
246 fast bursts are caused by a “plasma bubble”, the ion temperature and the plasma pressure are  
247 gradually increased from the onset of fast flow. However, during the presented interval, the  
248 observed plasma flow bursts were predominantly field-aligned. The associated temperatures  
249 explosively increased (did not increase) in case of the first (second) flow burst, and the plasma  
250 pressure enhancements were not seen at both flow onsets. After the first flow burst, the

251 enhancements of the plasma pressure were found because of the satellite entry to the plasma  
252 sheet.

253 Panels (b) and (c) of Figure 2 show zoomed-in plots of the plasma flow velocity and ground-  
254 based magnetic field perturbations measured at two ground observatories close to the TPA, for  
255 the first and second plasma flow bursts, respectively. The top two panels in each case show  
256 plasma flow velocity components in GSM coordinates and the x-directional components of  
257 plasma flow speed parallel and perpendicular to the local magnetic field, and the bottom two  
258 panels show ground magnetic field perturbations in the  $B_N$  (local magnetic north-south) and  $B_E$   
259 (local magnetic east-west) components measured at two representative ground magnetic  
260 observatories close to the TPA. Detailed information for the ground stations is listed in Table S2  
261 in order of geographic latitude. In the first plasma flow burst (panel b), the peaks of the  $V_x$  and  
262  $V_{\text{parax}}$  components, and those in the  $\Delta B_N$  components are seen at the same time, suggesting that  
263 the fast flows associated with magnetotail reconnection may trigger electric currents, and cause  
264 the variations of geomagnetic field. During the second flow burst interval, the geomagnetic field  
265 peaks were not seen as shown in panel (c). Therefore, at this stage of our analysis, it remains  
266 unclear whether or not electric currents which would disturb the geomagnetic field were induced  
267 by reconnection-associated fast plasma flows in this case. The summary and zoomed-in plasma  
268 velocity plots from Geotail observations of the opposite dawnside magnetotail are shown in the  
269 Supporting Information (Figure S2). Panel (d) shows the footpoints of the Geotail trajectory  
270 during the same time interval as panel (a) (1h 40m from 0:10 UT to 1:50 UT), which were  
271 calculated based on the Tsyganenko 96 empirical magnetic field model (Tsyganenko and Stern,  
272 1996), and projected onto IMAGE FUV-WIC data on 1:20 UT. The asterisk and diamond denote  
273 the start (0:10 UT) and end (1:50 UT) times of the Geotail footpoint trajectory. During the time  
274 interval of interest, the Geotail footpoints were located in the region of 74 degrees ~ 75 degrees  
275 MLat at ~ 22 hrs MLT, and were close to the “straight bar” part of TPA in the nightside.  
276 Therefore, it is expected that the fast plasma flows associated with magnetotail magnetic  
277 reconnection, which were observed during this time interval, may play a role in the formation of  
278 the nightside distorted TPA.

279

### 280 **3.3 Ionospheric Electric Currents Inferred from The Ground and Direct Evidence for** 281 **FACs**

282 When a shear in flow velocity exists between reconnection-associated earthward fast flows and  
283 slow magnetotail background flows is present, electric currents flowing along the geomagnetic  
284 field lines (Field-Aligned Currents: FACs) can be driven (Hasegawa and Sato, 1979; Birn and  
285 Hesse, 1991; Fairfield et al. 1999). These FACs are closely related to the auroral phenomena in  
286 the high-latitude atmosphere. In order to investigate this current system, an electric current map  
287 in the ionosphere is made based on the geomagnetic field variations beneath and in close  
288 proximity to the regions of growth of the nightside distorted (“L”-shaped) TPAs. These  
289 measurements were conducted using ground-based magnetic field observations from the  
290 SuperMAG ground observatory network (Gjerloev, 2012). Figure 3 shows the equivalent  
291 ionospheric current (EIC) distributions, projected onto the IMAGE FUV-WIC data in  
292 geomagnetic coordinates during time intervals spanning the two earthward flow bursts. The  
293 electric current maps are derived from the local magnetic north – south ( $B_N$ ) and east – west ( $B_E$ )  
294 components of the geomagnetic field perturbations, which were measured at the ground  
295 magnetic observatories beneath and in close proximity to the growth regions of the nightside  
296 distorted TPA. It is well-known that these ground magnetic disturbances are generated by the  
297 horizontal components of electric currents in the ionosphere (EIC) (Glassmeier et al. 1989). The  
298 orientation and scale of FACs can also be estimated based on the EIC distributions (Glassmeier  
299 et al. 1989; Morretto et al. 1997; Motoba et al. 2003, and references therein). The geomagnetic  
300 field perturbations were taken from 50-minute-high-pass filtered  $B_N$  and  $B_E$  components. Electric  
301 current orientations were estimated by rotating these geomagnetic field fluctuation components  
302 90 degrees clockwise (e.g., Glassmeier et al. 1989; Moretto et al. 1997). On the maps during both  
303 the first (A) and second (B) flow burst intervals, counter-clockwise current vortices were found,  
304 as indicated with magenta circular arrows. This counter-clockwise vortex-structured current  
305 suggests that FACs, oriented from the ionosphere toward the magnetotail, are caused by electron  
306 precipitation associated with reconnection-triggered plasma flow bursts, which were observed by  
307 Geotail. This result also suggests that the energized plasma (electrons) were conveyed by the  
308 magnetotail fast flows from the magnetotail to the ionosphere. The vortex spatial scale appears to  
309 be different between first and second interval. In panels (A), a “large-scale” vortex-like current  
310 structure is discerned by the electric current vectors measured at most observatories, which are  
311 mainly located in the dusk sector (westside) of the nightside distorted TPA, while “small-scale”  
312 current vortices with a similar rotational sense are indicated on the nightside part of the TPA

313 during the second interval (panels B). Neither vortex current structure showed any poleward  
314 (high-latitude) migration as the “L”-shaped TPA grew to the dayside.

315 The vortex-like ionospheric current structures, deduced from the geomagnetic field fluctuations,  
316 indicate that upward (from the ionosphere toward the magnetotail) FACs play an essential role in  
317 the formation of nightside distorted TPAs. To obtain clearer evidence for the presence of FACs  
318 associated with the TPAs, we investigated whether or not the DMSP (Defense Meteorological  
319 Satellite Program) satellites crossed the TPAs, and could measure the associated magnetic field  
320 to extract the current density along the magnetic field lines (FACs). From our 9 TPA events, we  
321 found that the DMSP-F13, -F14 and -F16 satellites crossed the dayside straightforward bar-  
322 shaped part of the “L”-shaped TPA, as seen on 28<sup>th</sup> October 2003.

323 Figure 4 shows the temporal variations of the current density parallel to the magnetic field lines  
324 ( $J_{\text{para}}$ ) derived by the DMSP magnetic field data, which are plotted against universal time (UT),  
325 and the DMSP tracking information, such as MLat, magnetic longitude (MLON) and MLT. The  
326 current density can be computed by applying Ampère’s law to the magnetic field perturbations,  
327 measured just before and after the DMSP-F13 (panel a), -F14 (panel b) and -F16 (panel c)  
328 crossings of the TPA. More detailed theory and techniques to derive the current density from the  
329 magnetic field data are described by Wang et al. (2005) and Lühr et al. (2016). During the DMSP  
330 crossing interval of each TPA (in each case less than 1 minute), bracketed by two magenta broken  
331 lines, negative  $J_{\text{para}}$  values were found. This indicates that upward FACs were flowing out of the  
332 TPA (Wang et al., 2005). The geomagnetic field measurements on ground showed large- and  
333 small-scale counter-clockwise vortex-like current structures beneath and in close proximity to  
334 the TPA, and negative  $J_{\text{para}}$  bays were found during the DMSP TPA crossings. These results  
335 indicate that upward FACs are a dominant source of the nightside distorted TPAs.

336

### 337 **3.4 Retreat of Reconnection Points**

338 The electric current vortices suggest that FACs may be essential to formation of the nightside  
339 distorted TPA. Here, we consider the “growth” of the TPA. According to the conventional model  
340 to explain the TPA formation based on nightside reconnection (Milan et al. 2005), which does  
341 not take into account the influence of FACs in the TPA formation, the reconnection points  
342 should retreat tailward as the TPA grows to the dayside. A summary plot of the Geotail  
343 observations shown in Figure 2 has already suggested the tailward retreat of the reconnection

344 point. To further support this scenario, we examine the geomagnetic field variations associated  
345 with the nightside distorted TPAs using ground-based observations. Figure 5(A) shows  
346 geomagnetic field observations at several ground magnetic observatories corresponding to the  
347 locations beneath or in close proximity to the regions of growth of a nightside distorted TPA  
348 (“L”-shaped TPA observed on 12<sup>th</sup> March 2002). All magnetic field data for the ground  
349 observatories were taken from the SuperMAG network (Gjerloev, 2012). Several magenta points  
350 labelled with numbers in the IMAGE FUV-WIC plots in panel (b) correspond to similarly  
351 labelled locations in geographical map (panel c). Panel (a) in figure 5(A) shows a stack plot of  
352 fluctuations in the local (magnetic) north-south geomagnetic field component ( $\Delta B_N$ ) at these  
353 observatories, which are shown by blue. The magnetic fluctuations are obtained by the  
354 subtraction of the average magnetic field over the time interval of interest from the raw magnetic  
355 field values. The fluctuation component at each station is plotted upon their averages as indicated  
356 by horizontal grey broken lines, and its peak during the “L”-shaped TPA intensification intervals,  
357 bracketed by two gold broken lines, is marked by magenta open circle. The plots are sorted in  
358 decreasing order of latitude. The magnetic field fluctuation component at the time of panel (b)  
359 (00:39:45 UT) is indicated by a vertical cyan solid line in the panel (a). The color code of the  
360 IMAGE FUV-WIC data in panel (b) is assigned according to ADU.

361 Figure 5(B) shows a scatter plot of the time-delay of the fluctuation peaks in the local  
362 (magnetic) north-south magnetic field component ( $\Delta B_N$ ) from the onset times of 5 nightside  
363 distorted TPAs at several ground magnetic observatories from geographical low- to high-  
364 latitudes. The detailed geomagnetic field plots and information on the ground magnetic  
365 observatories in the other four TPA events, except for the 12<sup>th</sup> March 2002 event, are shown in  
366 the Supporting Information (Figure S3). All peaks seen in the magnetic field fluctuation  
367 components were positive, implying enhancements of FACs flowing out of the ionosphere, that  
368 is, downflowing of electrons from the magnetotail. For three of the TPAs (2000/09/22,  
369 2001/12/31 and 2002/03/02), the magnetic peaks are clearly seen at later times for observatories  
370 with higher latitude, suggesting that the reconnection points (the source regions of the energetic  
371 electrons) were retreating further down-magnetotail, associated with the growth of the TPA to  
372 the dayside. This result supports not only the tail reconnection occurrence but also the retreat of  
373 the reconnection points. The average velocity of the reconnection point retreat can roughly be  
374 estimated based on the slope of a line of geographical latitude versus the time delay between the

375 magnetic peaks and the TPA onsets. We adopted a value of 1 degree = 110.95 km to convert a  
376 unit of geographic latitude (degree) to equatorial distance (km). The estimated reconnection  
377 point retreat velocity is summarized in the table in the top-right of the figure. The three TPAs  
378 mentioned above, with very apparent reconnection point retreats, had reconnection point retreat  
379 velocities within a range between about 1.2 km/s and 3.0 km/s. The others (2000/11/05 and  
380 2002/03/12) showed a much faster retreat speed (7.3 km/s and 12.3 km/s) because their magnetic  
381 field peaks appeared with much lower time lags, irrespective of the latitudes of the observatory  
382 locations.

### 383 **3.5 Persistence of Magnetotail Reconnection During the Northward IMF Interval**

384 We discuss the plasma flows and their patterns in the polar cap region measured by Super Dual  
385 Auroral Radar Network High Frequency (SuperDARN HF) radars (Greenwald et al. 1995;  
386 Chisham et al. 2007) during the nightside distorted TPA intervals, in order to obtain evidence for  
387 the persistence of magnetotail magnetic reconnection even under northward IMF conditions. The  
388 SuperDARN radars, which are located in the high-latitude regions in both Northern and Southern  
389 Hemispheres, provide line-of-sight ionospheric plasma flow velocity over much of the polar and  
390 auroral regions. These measurements, particularly obtained from nine SuperDARN radars in the  
391 Northern Hemisphere, have been used to produce high-latitude convection maps based on the  
392 “Map Potential” technique (Ruohoniemi and Baker, 1998). The line-of-sight velocity vectors are  
393 projected onto geomagnetic grids, and fitted to electrostatic potential solutions, which are  
394 described by a sixth order spherical harmonic expansion. Complementary flow data from a  
395 statistical model characterised by upstream IMF conditions (Ruohoniemi and Greenwald, 1996)  
396 is used to constrain the construction of the large-scale flow pattern in regions where the radars  
397 provide no measurements (Ruohoniemi and Baker, 1998).

398 Figure 6 presents 6 selected 2 minutes integrations of the northern hemispheric plasma flow  
399 streamlines and drift velocity vectors during the interval of a nightside distorted TPA (“J”-  
400 shaped TPA) observed on 31<sup>st</sup> December 2001. We overlay these flow velocity profiles onto the  
401 corresponding IMAGE FUV-WIC auroral imager data. Black regions indicate higher auroral  
402 luminosity, and the IMAGE observation time is shown at the top in each panel. The left, bottom  
403 and right sides in each panel correspond to 18h, 24h, and 6h in magnetic local time, respectively.  
404 The dotted semicircles indicate the magnetic latitude (MLat) range between 60 degrees and 80

405 degrees. During the growth of the “J”-shaped TPA, westward plasma flows, ranging between  
406 0.35 km/s and 0.85 km/s, were locally (although non-continuously) observed at the poleward  
407 edge of the midnight-sector main auroral oval, highlighted by magenta ovals. These flows were  
408 originally oriented toward the equator, but rotated toward the west at the poleward edge of the  
409 main auroral oval. They are highly suggestive of magnetic reconnection in the magnetotail,  
410 identified as “Tail Reconnection during IMF Northward and Non-substorm Intervals (TRINNIIs)”  
411 (Grocott et al. 2003, 2004) under dawnward IMF- $B_y$  conditions (see the IMF condition shown in  
412 Figure S1c) (Milan et al. 2005; Grocott et al. 2003, 2004). Therefore, at least, nightside  
413 reconnection was ongoing during the growth of the “J”-shaped TPA even under the northward  
414 IMF conditions, and should play a significant role in the nightside distorted TPA formation.

415

## 416 **4. Discussion**

### 417 *4.1 A Possible Formation Scenario of the Nightside Distorted TPA*

418 The conventional TPA formation model proposed by Milan et al. (2005) is based on the  
419 magnetospheric convection of closed magnetic fluxes formed by magnetotail reconnection. The  
420 ground-based observations revealed that the reconnection points retreated tailward with the  
421 poleward growth of the TPAs. Furthermore, the SuperDARN HF radar detected TRINNIIs, which  
422 are remote-sensing evidence for persistent magnetotail reconnection under the northward IMF  
423 conditions, being consistent with the framework of the conventional TPA formation model  
424 (Milan et al. 2005). However, our observations show that FACs can be generated by a plasma  
425 flow shear between the fast plasma flows triggered by nightside magnetic reconnection and  
426 background magnetospheric slow plasma flows, and appear to play an essential role in the  
427 formation of nightside distorted TPAs. In Figure 3, counter-clockwise vortex-like ionospheric  
428 current structures are detected by ground-based magnetic field observations beneath and in close  
429 proximity to the growth regions of the nightside distorted TPAs during the plasma flow bursts  
430 seen in the magnetotail. The current density component along magnetic field lines derived by the  
431 magnetic field perturbations during the DMSP satellite crossings of the TPA show significant  
432 negative bays in Figure 4. These observations suggest the presence of upward FACs associated  
433 with nightside distorted TPAs.

434 Taking into account these observations, we construct a model to illustrate nightside distorted

435 TPA (in particular, “L”-shaped TPA) formation. Figure 7 displays a schematic diagram of the  
436 possible formation process of an “L”-shaped TPA under positive (duskward) IMF- $B_y$  conditions.  
437 The main “bar-like” emissions of the nightside distorted TPAs are located on the dusk side under  
438 positive IMF- $B_y$  conditions as seen in Figure 1. The location of the “L”- (“J”)-shaped TPAs  
439 strongly depends on the IMF- $B_y$  sign; the relation between the location of the main TPA part and  
440 the IMF- $B_y$  polarity is the same as that for the “regular” TPA (Comnoco et al. 2002; Kullen et al.  
441 2002) (see the plots of the OMNI and Geotail-measured solar wind data in Figure S1). This  
442 model is depicted in terms of the configuration changes of magnetic field lines due to  
443 magnetospheric convection, FACs, reconnection-associated plasma flows, and the reconnection  
444 point retreat. The closed field lines formed by nightside reconnection are illustrated by thick blue  
445 solid curves, and the orange curves indicate the electric currents induced by the plasma flow  
446 shear between the background slow plasma flows and fast flows originating from magnetotail  
447 magnetic reconnection (blue arrows). FACs flowing out of the ionosphere toward the  
448 magnetotail constitute the “source” of the nightside distorted TPAs, being consistent with large-  
449 and small-scale electric current vortices beneath and in close proximity to the growth regions of  
450 the nightside distorted TPAs, and significant negative bays of the current density component  
451 along the magnetic field lines ( $J_{\text{para}}$ ) across the TPA. Magnetotail reconnection continues at the  
452 point denoted by red dots until the TPA completely forms, and associated closed field lines  
453 convect earthward. The reconnection location retreats further tailward from  $T_0$  to  $T_3$ , which are  
454 highlighted by the thick red arrows and the pink-shaded area, as the tip of the TPA approaches  
455 the dayside. This is because higher latitude field lines within the TPA have their nightside  
456 (equatorial crossing) positions further down-tail.

457 As the reconnection points retreat tailward, the TPA-associated closed flux tubes are  
458 contemporaneously twisted clockwise (counter-clockwise), depending on the dawnward  
459 (duskward) IMF- $B_y$  component. Meanwhile, the nightside plasma sheet undergoes an oppositely-  
460 oriented deformation (Tsyganenko et al. 2015; Tsyganenko and Fairfield, 2004), indicated by  
461 inclined red bar in Figure 7. The closed flux tube twisting is caused by the IMF- $B_y$  penetration,  
462 which produces “asymmetry” for the magnetic fields in the Northern and Southern Hemisphere,  
463 exerting “torque rotation” due to the electromagnetic force (Gosling et al. 1990; Cowley, 1981,  
464 1994). This results in the “L”- and “J”-shaped TPAs, corresponding to the ionospheric footpoints  
465 of these field lines in the Northern and Southern Hemispheres.



466 Before and during all nightside distorted TPAs examined in this study (listed in Table S1), the  
467 IMF- $B_z$  had been dominantly northward, however magnetotail reconnection appears to occur  
468 and, at least, persist during the TPA interval. This result is supported by significant  
469 enhancements in geomagnetic activity even under strong and persistent northward IMF- $B_z$   
470 conditions (Shi et al. 2012), and indicates that solar wind energy can enter the magnetosphere  
471 during the northward IMF intervals.

472 Zhu et al. (1997) suggests that the FACs associated with polar cap arcs (TPAs) indicate the  
473 presence of upward and downward current pairs. Chen and Wolf (1993) proposed a model of  
474 closure of upward and downward FACs in the dawn and dusk sectors, which are linked with the  
475 inertial currents in the magnetotail and the currents perpendicular to the magnetic field line in the  
476 ionosphere. In this model, it is considered that the magnetotail-ionosphere FACs were generated  
477 by the reconnection fast flows driven by a “plasma bubble”. However, in our model, TPA-  
478 associated magnetic field lines are closed by magnetotail reconnection, and FACs, which are the  
479 source of the TPA, may be caused by the flow shear due to the reconnection-associated fast  
480 plasma flows. This model simply explains that the nightside distorted TPA is comprised of only  
481 closed field lines that have been recently generated by nightside magnetic reconnection, and does  
482 not include the fate of other regions of closed fluxes which do not significantly contribute to the  
483 formation of the nightside distorted TPA.

484 Because the contribution of a “plasma bubble” for the observed fast flows seems to be small or  
485 insignificant, as shown in Figure 2, the bubble-associated current closure scenario is not well  
486 supported. In this study, sufficient data is unavailable to make an ionospheric current map that  
487 would reveal the global FAC profile in the Northern (Southern) Hemisphere. A series of studies  
488 based on a global MHD simulation (e.g., Tanaka et al. 2004; Watanabe et al. 2013) showed and  
489 discussed a large-scale profile of FAC distributions associated with TPA formation. Upward  
490 (downward) FACs can be developed in the sector opposite to the downward (upward) FACs, so  
491 that closed current systems are formed, but the development processes during the TPA growth  
492 are complicated. In particular, Watanabe et al. (2013) showed that multiple current closures,  
493 consisting of multiple upward and downward FACs, can be formed during the TPA growth. At  
494 this stage, the global FAC structure associated with the nightside distorted TPAs is not yet  
495 revealed with in-situ geomagnetic field measurements. This is a problem to be clarified in the  
496 future. In Figure S4, the SuperDARN radar data during this “L”-shaped TPA detected counter-

497 clockwise ionospheric plasma flows in the dawnside in the Northern Hemisphere. These plasma  
498 flow patterns (vortex-like plasma flows) may indicate that the clockwise ionospheric currents,  
499 that is, downward FACs, can be generated (e.g., Moretto et al. 1997; Motoba et al. 2003).  
500 However, in order to reveal the complete current system associated with the nightside distorted  
501 TPAs with greater certainty, a more extensive set of geomagnetic field observations is required.

#### 502 *4.2 Scale of Electric Current Vortex Associated with Nightside Distorted TPA*

503 The electric current vortices provide indicative evidence of FACs flowing out of the ionosphere  
504 to the magnetotail. However, their scales were found to be different between two nightside  
505 distorted TPA intervals: a large-scale vortex was seen during the first interval, whereas during  
506 the second “L”-shaped TPA interval, local small-scale vortices were found at the observatories  
507 near the TPA. Since these FACs were induced by the plasma flow shear, the velocity of the  
508 plasma flows associated with magnetotail reconnection would be a key physical parameter to  
509 determine the current vortex scale on the ground. Therefore, the current vortex scale might be  
510 roughly proportional to the plasma flow speed. The electric current vortex scale should become  
511 smaller, if the energy of plasma (electrons) released by magnetic reconnection in the magnetotail  
512 was dissipated upon the ionosphere (Tanskanen et al. 2002).

#### 513 *4.3 Formation of the Distortions at TPA Nightside Ends*

514 After the onset of nightside reconnection, the reconnection locations retreated tailward as the  
515 tips of the TPAs (in Northern and Southern Hemispheres) approach the dayside, and apparently  
516 become “stagnant points”, which are unaffected by magnetospheric convection. Furthermore, the  
517 closed flux tubes within the nightside distorted TPAs, which are generated by persistent  
518 nightside reconnection even under northward IMF conditions, are twisted, associated with the  
519 magnetotail deformation. During the growth of nightside distorted TPA under the significant  
520 IMF- $B_y$  conditions as the reconnection site moves further tailward, the tail deformation becomes  
521 larger and associated field lines are also twisted more strongly (Tsyganenko et al. 2015;  
522 Tsyganenko and Fairfield, 2004). Significantly, this twisting of field lines, caused by the IMF- $B_y$   
523 penetration (Gosling et al. 1990; Cowley, 1981, 1994), gives opposite chirality to the “J”- and  
524 “L”-shaped TPAs seen in the Northern and Southern Hemispheres, even though magnetotail  
525 magnetic reconnections occur at the “same” locations in the Northern and Southern Hemispheres  
526 (see Figure 7). In a previous study (Milan et al. 2005), it was considered that the nightside

527 magnetospheric deformation and field line twisting are only important in determining the TPA  
528 growth point in the nightside main auroral oval. Our scenario, however, emphasizes that they  
529 play an important role in determining not only the TPA morphology but also how the plasma  
530 (electrons) released by magnetotail reconnection are supplied to the ionosphere.

531

532

533

## 534 **5. Conclusions**

535 In this study, we have demonstrated that investigations of TPA morphology are important in  
536 assessing how the energy stored in the deformed magnetotail is released and supplied to the  
537 high-latitude atmosphere or ionosphere. In particular, we have shown that the nightside distorted  
538 TPA is a good remote-sensing diagnostic tool for monitoring global magnetospheric effects. The  
539 fundamental characteristics and the formation scenario of nightside distorted TPAs obtained  
540 through this study have clear potential for application to other planets. Namely, this study  
541 contributes to understanding the roles of the IMF and solar wind plasma in auroral processes,  
542 which can also occur at other planets of solar system. Hereafter, more detailed observations of  
543 the solar wind-magnetosphere-ionosphere coupling are required to better understand the process  
544 of nightside distorted TPA formation.

545 **Acknowledgments**

546 This work is supported by grants of the National Natural Science Foundation of China (NSFC  
547 41961130382, 41974189, and 41404131). B.H. is supported by the Belgian National Fund for  
548 Scientific Research (FNRS). A.W.D is supported by NSFC grant (41774172). A.G. is supported  
549 by STFC grant (ST/R000816/1) and NERC grants (NE/P001556/1 and NE/T000937/1). M.N.  
550 thanks Anthony T. Y. Lui for constructive and insightful discussion on our obtained results, and  
551 for modeling of the nightside distorted TPAs, and Chen-Yao Han for helping to draw Figure 7.  
552 Also, he thanks Yukinaga Miyashita for helping the MFC/FAC coordinate transformation of the  
553 Geotail plasma data, and the calculations of the Geotail footpoints on ionosphere. We thank the  
554 PIs of the SuperDARN radars for provision of the ionosphere flow data. SuperDARN is funded  
555 by the research agencies of Australia, China, Canada, France, Italy, Japan, South Africa, the U.  
556 K. and the U. S. For the ground magnetometer data we gratefully acknowledge: Intermagnet;  
557 USGS, Jeffrey J. Love; CARISMA, PI Ian Mann; CANMOS, Geomagnetism Unit of the  
558 Geological Survey of Canada; The S-RAMP Database, PI K. Yumoto and Dr. K. Shiokawa; The  
559 SPIDR database; AARI, PI Oleg Troshichev; The MACCS program, PI M. Engebretson; GIMA;  
560 MEASURE, UCLA IGPP and Florida Institute of Technology; SAMBA, PI Eftyhia Zesta; 210  
561 Chain, PI K. Yumoto; SAMNET, PI Farideh Honary; The IMAGE magnetometer network, PI L.  
562 Juusola; AUTUMN, PI Martin Connors; DTU Space, PI Anna Willer; South Pole and McMurdo  
563 Magnetometer, PI's Louis J. Lanzarotti and Alan T. Weatherwax; ICESTAR; RAPIDMAG;  
564 British Antarctic Survey; McMac, PI Dr. Peter Chi; BGS, PI Dr. Susan Macmillan; Pushkov  
565 Institute of Terrestrial Magnetism, Ionosphere and Radio Wave Propagation (IZMIRAN); GFZ,  
566 PI Dr. Juergen Matzka; MFGI, PI B. Heilig; IGFPAS, PI J. Reda; University of L'Aquila, PI M.  
567 Vellante; BCMT, V. Lesur and A. Chambodut; Data obtained in cooperation with Geoscience  
568 Australia, PI Marina Costelloe; AALPIP, co-PIs Bob Clauer and Michael Hartinger; SuperMAG,  
569 PI Jesper W. Gjerloev; Sodankylä Geophysical Observatory, PI Tero Raita; Polar Geophysical  
570 Institute, Alexander Yahnin and Yarolav Sakharov; Geological Survey of Sweden, Gerhard  
571 Schwartz; Swedish Institute of Space Physics, Mastoshi Yamauchi; UiT the Arctic University of  
572 Norway, Magnar G. Johnsen; Finish Meteorological Institute, PI Kirsti Kauristie.

573

574

575 **Data Availability**

576 IMAGE FUV-WIC data can be obtained by contacting the corresponding authors (M.N. and  
577 B.H.) and can also be accessed from <http://image.gsfc.nasa.gov>. SuperDARN data is freely  
578 provided for scientific research purposes and can be obtained from the SuperDARN data mirror  
579 (<http://bsslsuperdarn.nc.nerc-bas.ac.uk:8093/docs/>) or by contacting any of the SuperDARN PI  
580 research groups (<http://www.superdarn.ac.uk>). All SuperDARN radar data are processed by the  
581 software of fitacf v1.2 and make\_grid v1.14.er which are part of the Radar Software Toolkit  
582 (RST v4.2 <https://zenodo.org/record/1403226#.Xy0u7y3MxTY>). OMNI (ACE) IMF and solar  
583 wind plasma were obtained from Coordinated Data Analysis Web  
584 (<https://cdaweb.sci.gsfc.nasa.gov/index.html/>), provided by NASA Goddard Flight Space Flight  
585 Center (GSFCs) Space Physics Data Facility. The Geotail MGF and CPI data can be obtained  
586 from Data ARchives and Transmission System (DARTS), provided by the Center for Science-  
587 satellite Operation and Data Archive (C-SODA) at ISAS/JAXA  
588 (<http://darts.isas.jaxa.jp/about.html.en>). The ground magnetic field data used in this paper can be  
589 downloaded from the SuperMAG website (<http://supermag.jhuapl.edu/>). We also thank the  
590 World Data Centre for Geomagnetism, Kyoto University for accessing the data of *AU* and *AL*  
591 indices from <http://wdc.kugi.kyoto-u.ac.jp/index.html>. The triaxial fluxgate magnetometer data  
592 of DMSP (Defense Meteorological Satellite Program) with 1 second temporal resolution are  
593 accessible from the website of the database of the Coupling, Energetics and Dynamics of  
594 Atmospheric Regions (CEDAR)/Madrigal (<http://cedar.openmadrigal.org/list/> and  
595 <https://dmsp.bc.edu/html2/dmspssm.html>).

596 **References**

- 597 Angelopoulos, V., Baumjohann, W., Kennel, C. F., Coroniti, F. V., Kivelson, M. G., Pellat, R., et  
598 al. (1992), Bursty bulk flows in the inner central plasma sheet. *Journal of Geophysical*  
599 *Research: Space Physics*, 97, 4027 – 4039.
- 600 Angelopoulos, V., Kennel, C. F., Coroniti, F. V., Pellat, R., Kivelson, M. G., Walker, R. J.,  
601 Russell, C. T., Baumjohann, W., Feldman, W. C., and Gosling, J. T. (1994), Statistical  
602 characteristics of bursty bulk flow events, *Journal of Geophysical Research: Space Physics*, 99(  
603 A11), 21257– 21280, doi:10.1029/94JA01263.
- 604 Angelopoulos, V., et al. (1996), Multipoint analysis of a bursty bulk flow event on April 11,  
605 1985, *Journal of Geophysical Research: Space Physics*, 101(A3), 4967– 4989,  
606 doi:10.1029/95JA02722.
- 607 Angelopoulos, V., Runov, A., Zhou, X.-Z., Turner, D. L., Kiehas, S. A., Li, S.-S., Shinohara, I.  
608 (2013). Electromagnetic energy conversion at reconnection fronts. *Science*, 341(6153), 1478 –  
609 1482. <https://doi.org/10.1126/science.1236992>.
- 610 Baumjohann, W., Paschmann, G., and Cattell, C. A. (1989), Average plasma properties in the  
611 central plasma sheet, *Journal of Geophysical Research: Space Physics*, 94(A6), 6597– 6606,  
612 doi:10.1029/JA094iA06p06597.
- 613 Baumjohann, W., Paschmann, G., and Lühr, H. (1990), Characteristics of high-speed ion flows  
614 in the plasma sheet, *Journal of Geophysical Research: Space Physics*, 95(A4), 3801– 3809,  
615 doi:10.1029/JA095iA04p03801.
- 616 Baumjohann, W., Paschmann, G., Sckopke, N., Cattell, C. A., and Carlson, C. W. (1988),  
617 Average ion moments in the plasma sheet boundary layer, *Journal of Geophysical Research:*  
618 *Space Physics*, 93(A10), 11507 – 11520, doi:10.1029/JA093iA10p11507.
- 619 Birn, J., and Hesse, M., The substorm current wedge and field-aligned currents in MHD  
620 simulations of magnetotail reconnection, *J. Geophys. Res.: Space physics*, 96, A2, 1611 – 1618,  
621 (1991).
- 622 Black, D. I., Cosmic ray effects and faunal extinctions at geomagnetic field reversals, *Earth*  
623 *Planet. Sci. Lett.* 3, 225–236, (1967).

624

625 Chen, C. X., and Wolf, R. A. (1993), Interpretation of high - speed flows in the plasma sheet,  
626 Journal of Geophysical Research: Space Physics, 98(A12), 21409 – 21419,  
627 doi:10.1029/93JA02080.

628 Chisham, G., Lester, M., Milan, S. E., Freeman, M. P., Bristow, W. A., Grocott, A., McWilliams,  
629 K. A., Ruohoniemi, J. M., Yeoman, T. K., Dyson, P. L., Greenwald, R. A., Kikuchi, T.,  
630 Pinnock, M., Rash, J. P. S., Sato, N., Sofko, G. J., Villain, J.-P., and Walker, A. D. M., A  
631 decade of the Super Dual Auroral Radar Network (SuperDARN): Scientific achievements, new  
632 techniques and future directions. *Surveys in Geophysics*, 28(1), 33 – 109, (2007).

633 Cowley, S. W. H., Magnetospheric asymmetries associated with the y-component of the IMF,  
634 Planet. Space Sci., 29, 79 – 96, (1981).

635 Cowley, S. W. H., Earth's plasma environment: magnetic reconnection and its effect on  
636 magnetospheric fields and flows, *Philosophical Transaction: Physical Sciences and Engineering*,  
637 349, 1690, *The Solar-System: A Review of Results from Space Mission* (Nov. 15), 237 – 247,  
638 (1994).

639 Cumnock, J. A., Sharber, J. R., Heelis, R. A., Blomberg, L. G., Germany, G. A., Spann, J. F., and  
640 Coley, W. R., Interplanetary magnetic field control of theta aurora development, *J. Geophys.*  
641 *Res.: Space physics*, 107(A7), 1108, (2002).

642 Fairfield, D. H., Mukai, T., Brittnacher, M., Reeves, G. D., Kokubun, S., Parks, G. K., Nagai, T.,  
643 Matsumoto, H., Hashimoto, K., Gurnett, D. A., and Yamamoto, T., Earthward flow bursts in  
644 the inner magnetotail and their relation to auroral brightenings, AKR intensifications,  
645 geosynchronous particle injections and magnetic activity, *J. Geophys. Res.: Space physics*, 104,  
646 A1, 355 – 370, (1999).

647 Fear, R. C. and Milan, S. E., The IMF dependence of the local time of transpolar arcs:  
648 Implications for formation mechanism, *J. Geophys. Res.: Space physics*, 117(A03213),  
649 (2012a).

650 Fear, R. C. and Milan, S. E. Ionospheric flows relating to transpolar arc formation, *J. Geophys.*  
651 *Res.: Space physics*, 117, A09230, (2012b).

652 Frank, L. A., Craven, J. D., Burch, J. L., and Winningham, J. D., Polar views of the Earth's  
653 aurora with Dynamics Explorer, *Geophys. Res. Lett.*, 9(9), 1001 – 1004, (1982).

654 Gjerloev, J. W., The SuperMAG data processing technique, *J. Geophys. Res.: Space physics*,  
655 117, A09213, (2012).

656 Glassmeier, K. -H., Hönisch, M., and Untiedt, J., Ground-based and spacecraft observations of  
657 traveling magnetospheric convection twin vortices, *Journal of Geophysical Research: Space*  
658 *physics*, 94, 2520–2528, (1989).

659 Glassmeier, K. -H., Richter, O., Vogt, J., Möbus, P., and Schwab, A., The Sun, geomagnetic  
660 polarity transitions, and possible biospheric effects: review and illustrating model. *Int. J.*  
661 *Astrobiol.*, 8, 147–159, (2009).

662 Glassmeier, K. -H., and Vogt, J., Magnetic polarity transitions and biospheric effects, *Space Sci.*  
663 *Rev.*, 155, 1-4, 387 – 410, (2010).

664 Gosling, J. T., Thomsen, M. F., Bame, S. J., Elphic, R. C., and Russell, C. T., Plasma flow  
665 reversals at the dayside magnetopause and the origin of asymmetric polar cap convection, *J.*  
666 *Geophys. Res.: Space physics*, 95(A6), 8073 – 8084, (1990).

667 Greenwald, R. A., Baker, K. B., Dudeney, J. R., Pinnock, M., Jones, T. B., Thomas, E. C.,  
668 Villain, J. -P., Cerisier, J. -C., Senior, C., Hanuise, C., Hunsucker, R. D., Sofko, G., Koehler, J.,  
669 Nielsen, E., Pellinen, R., Walker, A. D. M., Sato, N., and Yamagishi, H., DARN/SuperDARN:  
670 A global view of high latitude convection, *Space Sci. Rev.*, 71(1-4), 761 – 796, (1995).

671 Grocott, A., Cowley, S. W. H., and Sigwarth, J. B., Ionospheric flow during extended intervals  
672 of northward but  $B_Y$ -dominated IMF, *Ann. Geophys.*, 21(2), 509 – 538, (2003).

673 Grocott, A., Badman, S. V., Cowley, S. W. H., Yeoman, T. K., and Cripps, P. J., The influence  
674 of IMF  $B_Y$  on the nature of the nightside high-latitude ionospheric flow during intervals of  
675 positive IMF  $B_Z$ , *Ann. Geophys.*, 22(5), 1755 – 1764, (2004).

676 Grocott, A., Yeoman, T. K., Milan, S. E., Amm, O., Frey, H. U., Juusola, L. et al., Multi-scale  
677 observations of magnetotail flux transport during IMF-northward non-substorm intervals. *Ann.*  
678 *Geophys.*, 25, 1709-1720. doi:10.5194/angeo-25-1709-2007, (2007).

679 Hasegawa, A., and Sato, T., Generation of Field Aligned Current During Substorm. In: Akasofu  
680 SI. (eds) *Dynamics of the Magnetosphere*. Astrophysics and Space Science Library (A Series of



681 Books on the Recent Developments of Space Science and of General Geophysics and  
682 Astrophysics Published in Connection with the Journal Space Science Reviews), 78. Springer,  
683 Dordrecht, (1979).

684 Heppner, J. P., and Maynard, N. C., Empirical high-latitude electric field models, *J. Geophys.*  
685 *Res.: Space physics*, 92, 4467 – 4489, (1987).

686 Kaymaz, Z., Siscoe, G., Luhmann, J. G., Fedder, J. A., and Lyon, J. G., Interplanetary magnetic  
687 field control of magnetotail field: IMP 8 data and MHD model compared, *J. Geophys. Res.:*  
688 *Space physics*, 100, A9, 17,163 – 17,172, (1995).

689 Kullen, A., Brittnacher, M., Cumnock, J. A., and Blomberg, L. G., Solar wind dependence of the  
690 occurrence and motion of polar auroral arcs: A statistical study, *J. Geophys. Res.: Space*  
691 *physics*, 107(A11), 1362, (2002).

692 Kullen, A., Fear, R. C., Milan, S. E., Carter, J. A., and Karlsson, T., The statistical difference  
693 between bending arcs and regular polar arcs, *J. Geophys. Res.: Space physics*, 120, (2015).

694 Lühr, H., Huang, T., Wing, S., Kervalishvili, G., Rauberg, J., and Korth, H. (2016), Filamentary  
695 field-aligned currents at the polar cap region during northward interplanetary magnetic field  
696 derived with the Swarm constellation, *Ann. Geophys.*, 34, 901 – 915,  
697 <https://doi.org/10.5194/angeo-34-901-2016>.

698 Milan, S. E., Hubert, B., and Grocott, A., Formation and motion of a transpolar arc in response to  
699 dayside and nightside reconnection, *J. Geophys. Res.: Space physics*, 110, A01212, (2005).

700 Mende, S. B., Heetderks, H., Frey, H. U., Lampton, M., Geller, S. P., Habraken, S., Renotte, E.,  
701 Jamar, C., Rochus, P., Spann, J., Fuselier, S. A., Gerard, J. -C., Gladstone, R., Murphree, S.,  
702 and Cogger, L., Far ultraviolet imaging from the IMAGE spacecraft: 1. System design, *Space*  
703 *Sci. Rev.*, 91, 243 – 270, (2000).

704 Mende, S. B., Heetderks, H., Frey, H. U., Lampton, M., Geller, S. P., Abiad, R., Siegmund, O.  
705 H. W., Tremsin, A. S., Spann, J., Dougani, H., Fuselier, S. A., Magoncelli, A. L., Bumala, M.  
706 B., Murphree, S., and Trondsen, T., Far ultraviolet imaging from the IMAGE spacecraft: 2.  
707 Wideband FUV imaging, *Space Sci. Rev.*, 91, 271 – 285, (2000).

708 Mende, S. B., Heetderks, H., Frey, H. U., Stock, J. M., Lampton, M., Geller, S. P., Abiad, R.,  
709 Siegmund, O. H. W., Habraken, S., Renotte, E., Jamar, C., Rochus, P., Gerard, J. -C., Sigler, R.,

710 and Lauche, H., Far ultraviolet imaging from the IMAGE spacecraft: 3. Spectral imaging of  
711 Lyman- $\alpha$  and OI 135.6 nm, *Space Sci. Rev.*, 91, 287 – 318, (2000).

712 Motoba, T., Kikuchi, T., Okuzawa, T., and Yumoto, K. (2003), Dynamical response of the  
713 magnetosphere-ionosphere system to a solar wind dynamic pressure oscillation, *Journal of*  
714 *Geophysical Research: Space Physics*, 108(A5), 1206, doi:10.1029/2002JA009696.

715 Moretto, T., Friis-Christensen, E., Lühr, H., and Zesta, E. (1997), Global perspective of  
716 ionospheric traveling convection vortices: Case studies of two Geospace Environmental  
717 Modeling events, *Journal of Geophysical Research: Space Physics*, 102(A6), 11597– 11610,  
718 doi:10.1029/97JA00324.

719 Nagai, T., Shinohara, I., Fujimoto, M., Hoshino, M., Saito, Y., Machida, S., and Mukai, T.  
720 (2001), Geotail observations of the Hall current system: Evidence of magnetic reconnection in  
721 the magnetotail, *Journal of Geophysical Research: Space Physics*, 106(A11), 25929 – 25949,  
722 doi:10.1029/2001JA900038.

723 Nishida, A., Mukai, T., Yamamoto, T., Saito, Y., Kokubun, S., and Maezawa, K., GEOTAIL  
724 observation of magnetospheric convection in the distant tail at 200  $R_E$  in quiet times, *J.*  
725 *Geophys. Res.: Space physics*, 100, A12, 23,663 – 23,675, (1995).

726 Nishida, A., Mukai, T., Yamamoto, T., Kokubun, S., and Maezawa, K., A unified model of the  
727 magnetotail convection in geomagnetically quiet and active times *J. Geophys. Res.: Space*  
728 *physics*, 103, A3, 4409 – 4418, (1998).

729 Nowada, M., Fear, R. C., Grocott, A., Shi, Q. -Q., Yang, J., Zong, Q. -G., Wei, Y., Fu, S. -Y., Pu,  
730 Z. -Y., Mailyan, B., and Zhang, H., Subsidence of ionospheric flows triggered by magnetotail  
731 magnetic reconnection during transpolar arc brightening, *J. Geophys. Res.: Space physics*, 123,  
732 (2018).

733 Petrukovich, A. A., Sergeev, V. A., Zelenyi, L. M., Mukai, T., Yamamoto, T., et al. (1998). Two  
734 spacecraft observations of a reconnection pulse during an auroral breakup. *Journal of*  
735 *Geophysical Research*, 103(A1), 47–59. <https://doi.org/10.1029/97JA02296>.

736 Pitkänen, T., Hamrin, M., Norqvist, P., Karlsson, T., and Nilsson, H., IMF dependence of the  
737 azimuthal direction of earthward magnetotail fast flows, *Geophys. Res. Lett.*, 40, 5598, (2013).

738 Pitkänen, T., Hamrin, M., Norqvist, P., Karlsson, T., Nilsson, H., Kullen, A., Imber, S. M., and

739 Milan, S. E., Azimuthal velocity shear within an earthward fast flow: Further evidence for  
740 magnetotail untwisting, *Ann. Geophys.*, 33, 245, (2015).

741 Pitkänen, T., Hamrin, M., Karlsson, T., Nilsson, H., and Kullen, A., On IMF By-induced dawn-  
742 dusk asymmetries in earthward convective fast flows. In S. Haaland, A. Runov, & C. Forsyth  
743 (Eds.), *Dawn-dusk asymmetries in planetary plasma environments*, Geophysical Monograph  
744 Series, 95–106, Hoboken, NJ: John Wiley, (2017).

745 Ruohoniemi, J. M., and Baker, K. B., Large-scale imaging of high-latitude convection with  
746 Super Dual Auroral Radar Network HF radar observations, *J. Geophys. Res.: Space physics*,  
747 103(A9), 20797 – 20811, (1998).

748 Ruohoniemi, J. M., and Greenwald, R. A., Statistical patterns of high-latitude convection  
749 obtained from Goose Bay HF radar observations, *J. Geophys. Res.: Space physics*, 101(A10),  
750 21743 – 21763, (1996).

751 Shi, Q. -Q., Zong, Q. -G., Fu, S. -Y., Dunlop, M. W., Pu, Z. -Y., Parks, G. K., Wei, Y., Li, W. -  
752 H., Zhang, H., Nowada, M., Wang, Y. B., Sun, W. -J., Xiao, T., Rème, H., Carr, C., Fazakerley,  
753 A. N., and Lucek, E., Solar wind entry into the high-latitude terrestrial magnetosphere during  
754 geomagnetically quiet times. *Nat. Commun.*, 4, 1466, (2013).

755 Shi, X. -F., Zong, Q. -G., and Wang, Y. -F., Comparison between the ring current energy  
756 injection and decay under southward and northward IMF  $B_z$  conditions during geomagnetic  
757 storms, *Sci. China Tech. Sci.*, 55, 10, 2769 – 2777, (2012).

758 Tanaka, T., T. Obara, and M. Kunitake (2004), Formation of the theta aurora by a transient  
759 convection during northward interplanetary magnetic field, *Journal of Geophysical Research:*  
760 *Space Physics*, 109, A09201, doi:10.1029/2003JA010271.

761 Tanskanen, E., Pulkkinen, T. I., Koskinen, H. E. J., and Slavin, J.A., Substorm energy budget  
762 during low and high solar activity: 1997 and 1999 compared, *J. Geophys. Res.: Space Physics*,  
763 107(A6), 1086, (2002).

764 Tenfjord, P., Østgaard, N., Snekvik, K., Laundal, K. M., Reistad, J. P., Haaland, S., and Milan, S.  
765 E., How the IMF  $B_y$  induces a  $B_y$  component in the closed magnetosphere and how it leads to  
766 asymmetric currents and convection patterns in the two hemispheres, *J. Geophys. Res.: Space*  
767 *Physics*, 120, 9368 – 9384, (2015).

769 Tenfjord, P., Østgaard, N., Haaland, S., Snekvik, K., Laundal, K. M., Reistad, J. P., Strangeway,  
770 R., Milan, S. E., Hesse, M., and Ohma, A., How the IMF  $B_y$  induces a local  $B_y$  component  
771 during northward IMF  $B_z$  and characteristic timescales, *J. Geophys. Res.: Space physics*, 123,  
772 (2018).

773 Tsyganenko, N. A., and Stern, D. P. (1996), Modeling the Global Magnetic Field of the Large-  
774 Scale Birkeland Current Systems, *J. Geophys. Res.: Space Physics*, 101, 27187 - 27198.

775 Tsyganenko, N. A., Andreeva, V. A., and Gordeev, E. I. (2015), Internally and externally  
776 induced deformations of the magnetospheric equatorial current as inferred from spacecraft data,  
777 *Ann. Geophys.*, 33, 1 – 11.

778 Tsyganenko, N. A., and Fairfield, D. H. (2004), Global shape of the magnetotail current sheet as  
779 derived from Geotail and Polar data, *J. Geophys. Res.: Space physics*, 109(A03218).

780 Tsyganenko, N. A., and Sitnov, M. I. (2005), Modeling the dynamics of the inner magnetosphere  
781 during strong geomagnetic storms, *J. Geophys. Res.: Space physics*, 110 (A3), A03208.

782 Wang, C. -P., Liu, Y. -H., Xing, X., Runov, A., Artemyev, A., and Zhang, X., (2020). An event  
783 study of simultaneous earthward and tailward reconnection exhaust flows in the Earth's midtail,  
784 *Journal of Geophysical Research: Space Physics*, 125, e2019JA027406,  
785 <https://doi.org/10.1029/2019JA027406>.

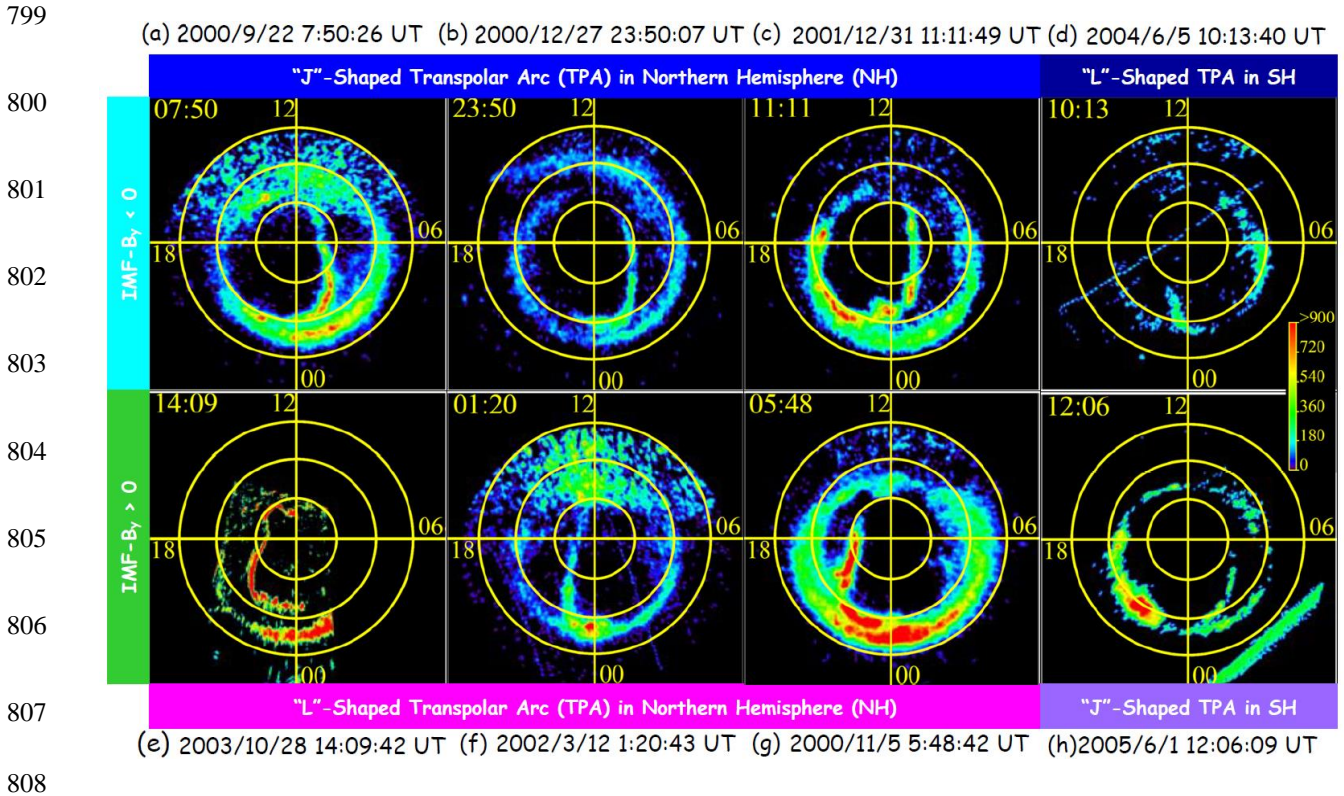
786 Wang, H., Lühr, H., and Ma, S. -Y. (2005), Solar zenith angle and merging electric field control  
787 of field-aligned currents: A statistical study of the Southern Hemisphere, *Journal of*  
788 *Geophysical Research: Space Physics*, 110, A03306, doi:10.1029/2004JA010530.

789 Watanabe, M., Sakito, S., Tanaka, T., Shinagawa, H., and Murata, K. T. (2014), Global MHD  
790 modeling of ionospheric convection and field-aligned currents associated with IMF  $B_y$   
791 triggered theta auroras, *Journal of Geophysical Research: Space Physics*, 119, 6145–6166,  
792 doi:10.1002/2013JA019480.

793 Wei, Y., Pu, Z. -Y., Zong, Q. -G., Wan, W.-X., Ren, Z. -P., Fraenz, M., Dubinin, E., Tian, F., Shi,  
794 Q. -Q., Fu, S. -Y., Hong, M. -H., Oxygen escape from the Earth during geomagnetic reversals:  
795 Implications to mass extinction, *Earth Planet. Sci. Lett.*, 394, 94-98, (2014).

796 Zhu, L., Schunk, R. W., and Sojka, J. J. (1997), Polar cap arcs: A review, *J. Atmos. Sol.-Terr.*  
797 *Phys*, 59, 10, 1087 – 1126.

798 **Figures and Captions**



809 Figure 1: IMAGE-FUV-WIC data plots of selected 8 nightside distorted TPAs are shown. The  
 810 upper panels (a) to (c) display the “J”-shaped TPAs whose nightside ends are distorted toward  
 811 midnight or pre-midnight, observed in the Northern Hemisphere under negative (dawnward)  
 812 IMF-B<sub>y</sub> conditions. Panels (e) to (g) show the “L”-shaped TPAs with the nightside ends distorted  
 813 toward midnight or post-midnight during positive (duskward) IMF-B<sub>y</sub> intervals. Panels (d) and  
 814 (h) show an “L”-shaped, and a “J”-shaped TPAs in the Southern Hemisphere during negative  
 815 and positive IMF-B<sub>y</sub> intervals. These panels are orientated in the same way, with noon  
 816 (midnight) at the top (bottom), and dusk (dawn) on the left (right) of each plot. The yellow  
 817 concentric circles show the magnetic latitude (MLat) from 60 degrees to 80 degrees. The color  
 818 code is assigned according to Analogic-Digital Units (ADU), which is comparable to a detector  
 819 count rate, being proportional to the observed auroral brightness (accounting for the spectral  
 820 response of the instrument).

821  
822  
823



848 during a 1 h 40 minute interval from 0:10 UT to 1:50 UT. The panels from top to bottom show  
849 the IMF- $B_y$  and  $-B_z$  components in GSM coordinates, solar wind dynamic pressure, the three  
850 components of the duskside magnetotail magnetic field in GSM, associated magnetic field  
851 elevation angle, GSM-X and x-directional components of the plasma flow velocity parallel and  
852 perpendicular to the local magnetic field, the GSM-Y and -Z components of the magnetotail  
853 plasma velocity, the plasma (ion) temperature, and magnetic and plasma pressures, respectively.  
854 Two clear intensified intervals of the “L”-shaped TPA are each bracketed with two gold broken  
855 lines. Zoomed-in plasma flow velocity in GSM-X and x-directional components of parallel and  
856 perpendicular to the local magnetic field, including significant  $V_x$  enhancements which suggest  
857 an earthward plasma flow burst, and corresponding geomagnetic field variations observed at two  
858 representative ground observatories close to the “L”-shaped TPAs are shown in panels (b) and  
859 (c). The geomagnetic field fluctuations are calculated by a subtraction of the magnetic field  
860 average during the presented interval from the observed magnetic field data. Panel (d) shows the  
861 footpoints of the Geotail trajectory during 1 hour 40 minutes from 0:10 UT (asterisk) to 1:50 UT  
862 (diamond), projected onto the IMAGE FUV-WIC data observed on 1:20 UT, using the  
863 Tsyganenko 96 magnetic field empirical model (Tsyganenko and Stern, 1996).

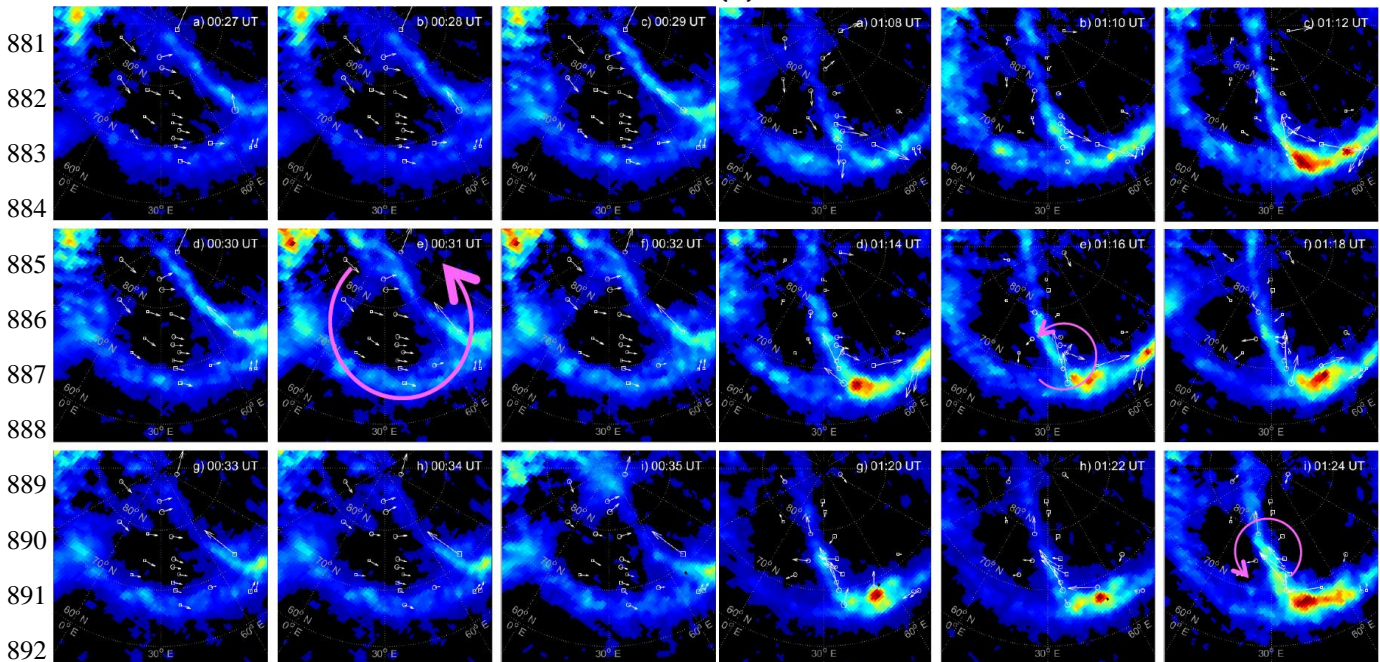
864  
865  
866  
867  
868  
869  
870  
871  
872  
873  
874  
875  
876  
877  
878



879

880 (A)

(B)



893 Figure 3: The vortex-like electric current structures detected by ground magnetic observatories  
894 beneath and in close proximity to the growth region of the “L”-shaped TPA from 00:27 UT to  
895 00:35 UT with one minute time-step (panels A), and from 01:08 UT to 01:24 UT with two  
896 minutes time-step (panels B) on 12<sup>th</sup> March 2002 are shown. The electric current vectors are  
897 derived based on the ground magnetic field fluctuations during the time intervals including the  
898 first (a) and second (b) plasma earthward flow bursts, projected onto IMAGE FUV-WIC data in  
899 geomagnetic coordinates. Squares and circles with different sizes denote the polarity (positive  
900 and negative) and scale of the vertical directional magnetic field fluctuation component ( $\Delta B_z$ ).  
901 Magenta circle arrows denote large- and small-scale -clockwise current vortices as seen in panels  
902 A and B, respectively.

903

904

905

906

907

908

909

910

911

912

913

914

915

916

917

918

919

920

921

922

923

924

925

926

927

928

929

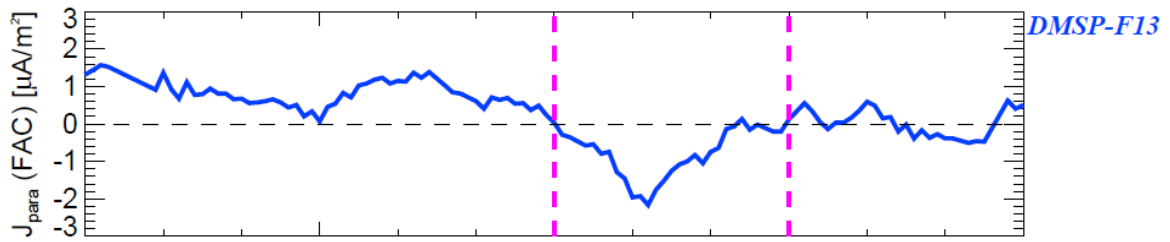
930

931

932

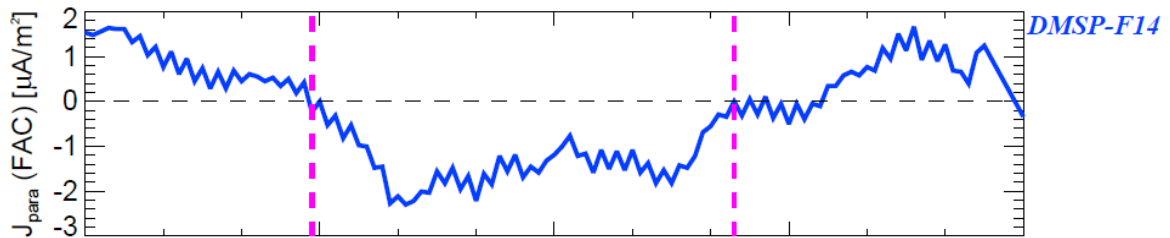
**FACs during the "L"-shaped TPA  
Observed by DMSP-F13,-F14 and -F16 on 2003/10/28**

(a)



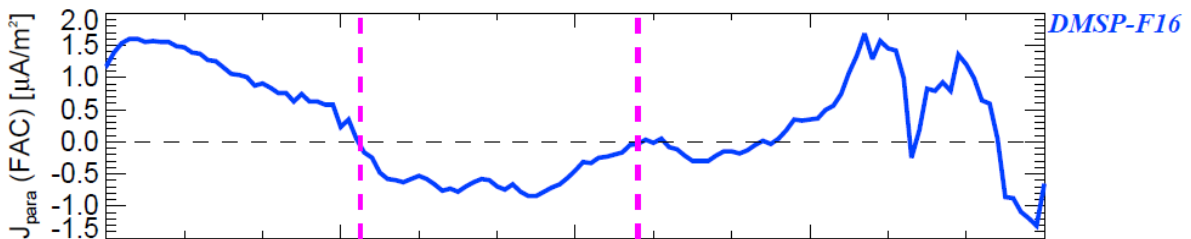
<i>UT</i>	13:44:00	13:44:30	13:45:00	13:45:30	13:46:00
<i>MLAT</i>	79.7800	81.1700	82.5300	83.3700	84.4800
<i>MLON</i>	107.950	102.010	95.3700	86.7600	75.2800
<i>MLT</i>	16.6203	16.2309	15.7885	15.1778	14.3636

(b)



<i>UT</i>	14:01:30	14:02:00	14:02:30	14:03:00	14:03:30
<i>MLAT</i>	80.8600	81.8400	82.3700	82.7600	82.7300
<i>MLON</i>	102.110	93.8600	82.1100	73.2900	60.2400
<i>MLT</i>	16.5114	15.9717	15.1567	14.5455	13.6281

(c)



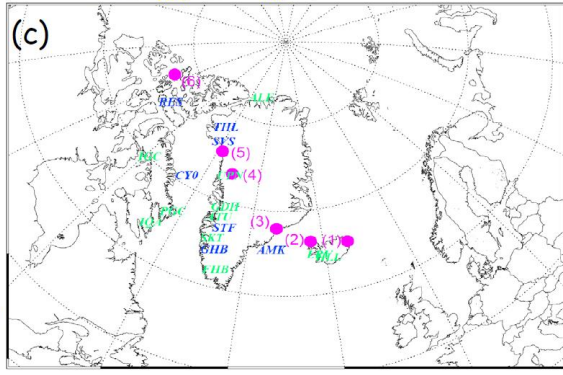
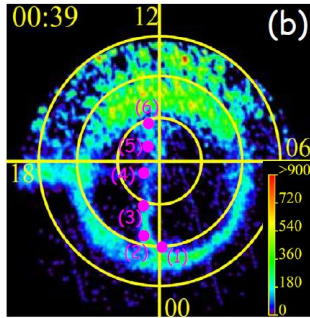
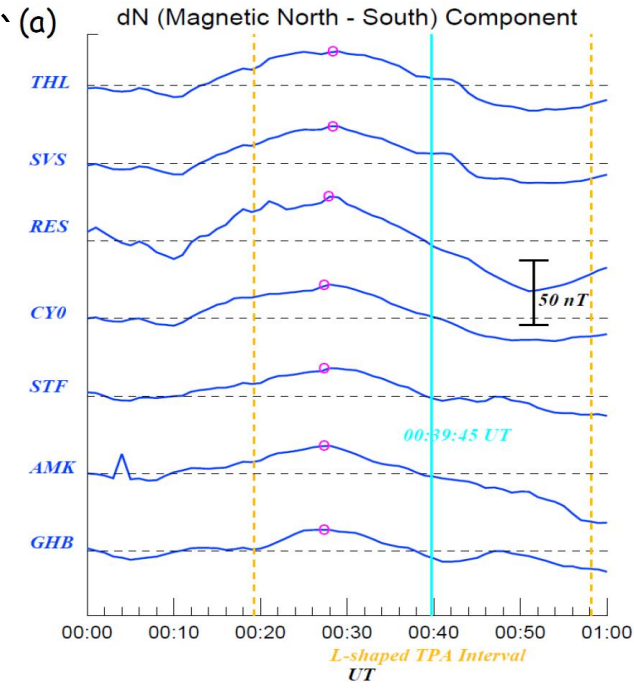
<i>UT</i>	13:59:00	13:59:30	14:00:00	14:00:30	14:01:00
<i>MLAT</i>	80.8400	81.4200	81.9500	81.9100	81.8000
<i>MLON</i>	97.7800	87.7600	77.4000	65.3600	53.5800
<i>MLT</i>	16.1889	15.4930	14.7697	13.9275	13.1019

933 Figure 4: The temporal variations of the current density along the magnetic field lines ( $J_{para}$ , i.e.,  
 934 field-aligned current: FAC) against the universal time (UT), magnetic latitude (MLAT),  
 935 magnetic longitude (MLON), and magnetic local time (MLT) are shown. All  $J_{para}$  values are  
 936 derived from the magnetic field fluctuations observed during the DMSP-F13 (panel a) -F14  
 937 (panel b), and -F16 (panel c) crossings of the dayside straightforward bar-shaped part of the "L"-  
 938 shaped TPA, observed on 28<sup>th</sup> October 2003. The detailed theory and methodology to deduce the  
 939  $J_{para}$  values from the magnetic field data are given in Wang et al. (2005) and Lühr et al. (2016).

940 The TPA crossing time intervals of the three DMSP satellites are bracketed by two magenta  
941 broken lines.

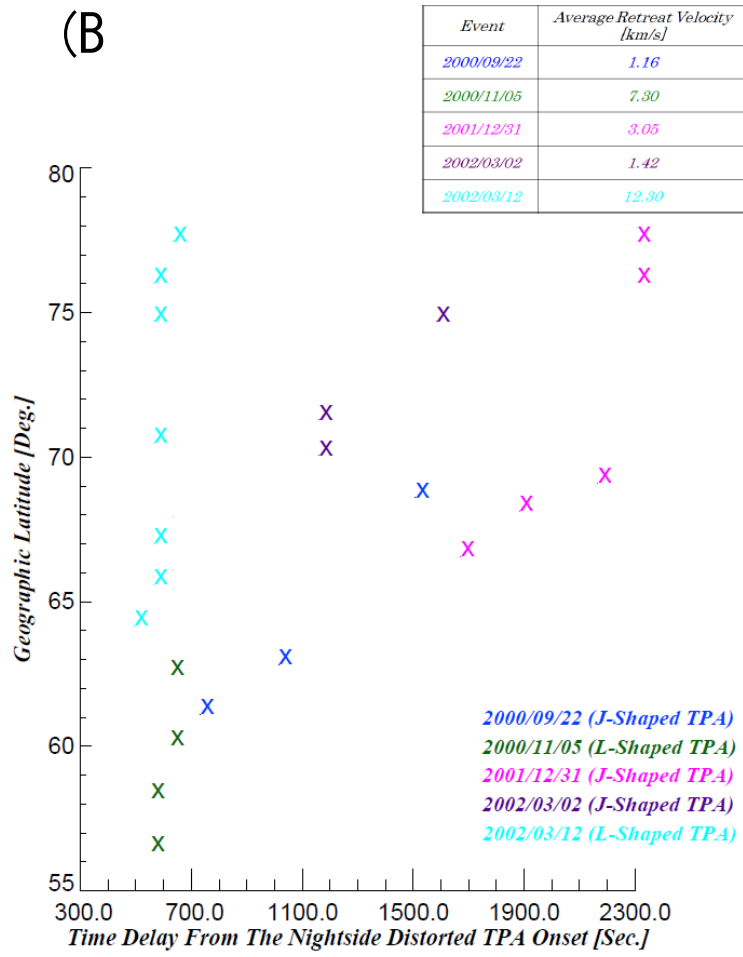
942  
943  
944  
945  
946  
947  
948  
949  
950  
951  
952  
953  
954

(A)



955  
956  
957  
958  
959  
960  
961  
962  
963  
964  
965  
966  
967  
968  
969

(B)



970 Figure 5: (A) The plots of in-situ geomagnetic magnetic field variations beneath and in close  
971 proximity to the growth regions of a nightside distorted TPA (“L”-shaped TPA observed on 12<sup>th</sup>  
972 March 2001) are displayed. Panels (a) to (c) show the magnetic field at several ground magnetic  
973 observatories corresponding to the locations beneath or in close proximity to the regions of  
974 growth of the “L”-shaped TPA. Several magenta points labelled with numbers in the IMAGE  
975 FUV-WIC plots (panel b) correspond to similarly labelled locations in geographical map (panel  
976 c). Panel (a) shows the plots of fluctuations in the local magnetic north-south magnetic field  
977 component ( $\Delta B_N$ ) at these observatories highlighted by blue. The fluctuation component, which  
978 was obtained by the subtraction of average magnetic field over the time interval of interest from  
979 the observed magnetic field values at each station, is plotted upon their averages (horizontal grey  
980 broken lines), and its peak during the “L”-shaped TPA intensification intervals (vertical gold  
981 broken lines), is marked by magenta open circle. The plots are sorted in decreasing order of  
982 latitude. The magnetic field fluctuation component at the time of panel (b) is indicated by a  
983 horizontal solid line in the panel. The color code of the IMAGE FUV-WIC data is assigned  
984 according to ADU. (B) The relationship between the magnetic peaks observed at several ground  
985 observatories beneath and in close proximity to the growth regions of the 5 nightside distorted  
986 TPAs from geographical low- to high-latitudes, and the time delays from the 5 TPA onset times  
987 to the magnetic peak times is shown. The magnetic field peaks seen in the local magnetic north-  
988 south magnetic field component ( $\Delta B_N$ ) are used. A rough estimation of the reconnection point  
989 retreat speed, which was calculated based on the slope of a line of geographical latitude versus  
990 the time delay between the magnetic peaks and the TPA onsets, is summarized in the table in the  
991 top-right of the panel. We adopted a value of 1 degree = 110.95 km to convert a unit of  
992 geographic latitude (degree) to equatorial distance (km).

993

994

995

996

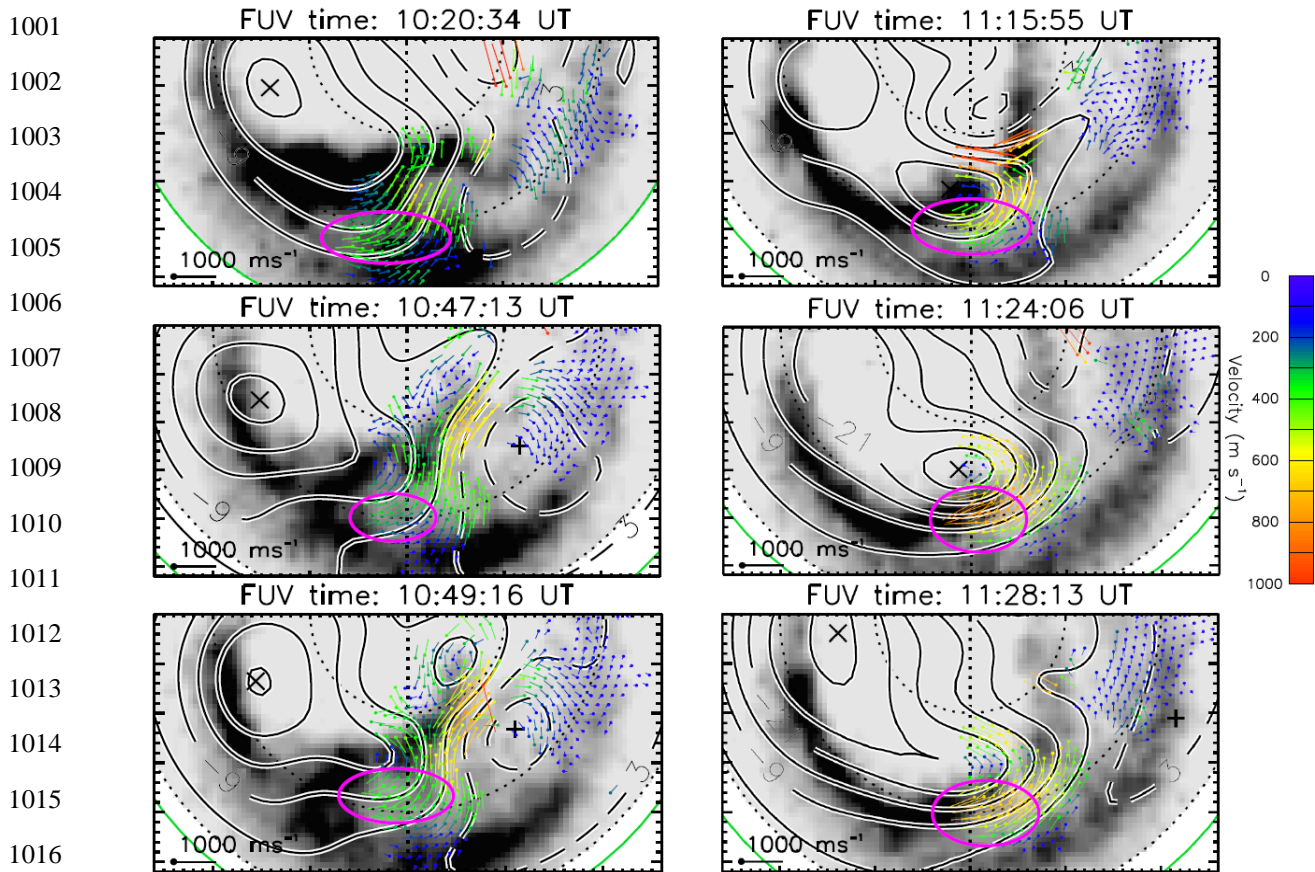
997

998

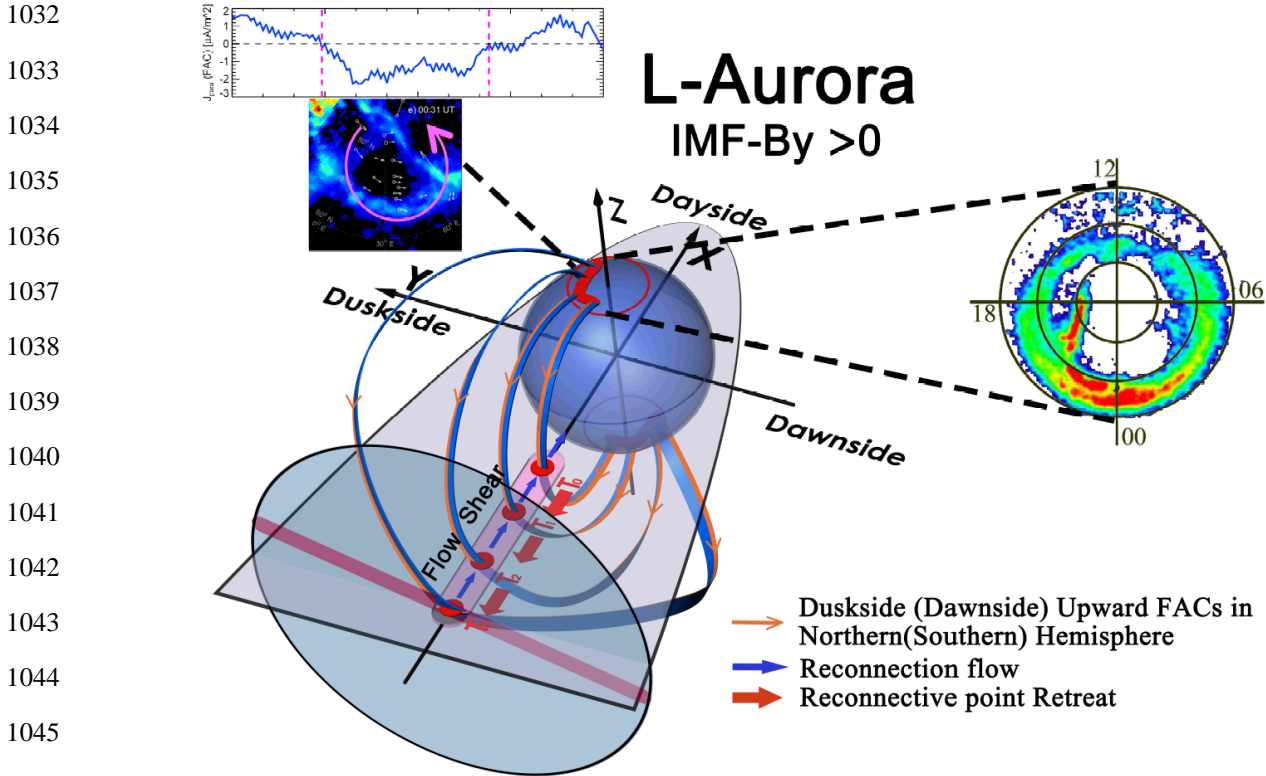
999

1000





1017 Figure 6: The nightside polar cap plasma flow streamlines and their line-of-sight velocity vectors  
 1018 measured by SuperDARN in the Northern Hemisphere, overlaid by the IMAGE FUV-WIC  
 1019 auroral image data, are shown. The dotted circles indicate the magnetic latitude (MLat) from 60  
 1020 degrees to 80 degrees. The left, bottom and right sides in each panel show 18h, 24h and 6h in  
 1021 magnetic local time (MLT), respectively. The time resolutions of the SuperDARN and IMAGE  
 1022 FUV-WIC data are 2 minutes. These streamlines and velocity vectors are projected onto the  
 1023 geomagnetic grids, and positive (maximum denoted by a plus) and negative (minimum shown  
 1024 with a cross) electrostatic potential models, which are controlled by the IMF conditions, as  
 1025 shown with black solid and broken contours on dawn and dusk. The equipotential values are also  
 1026 overlaid. The green curves show the lower latitude limit of the plasma convection pattern in the  
 1027 polar cap (Heppner and Maynard, 1987), determined from the line-of-sight plasma velocities  
 1028 measured by the radars. Each dot shows a SuperDARN radar measurement. The length of the  
 1029 vectors and color code are assigned according to the flow orientation and speed in units of m/s.  
 1030 Westward “Tail Reconnection during IMF Northward and Non-substorm Interval” (TRINNI)  
 1031 flows are marked with magenta ovals.

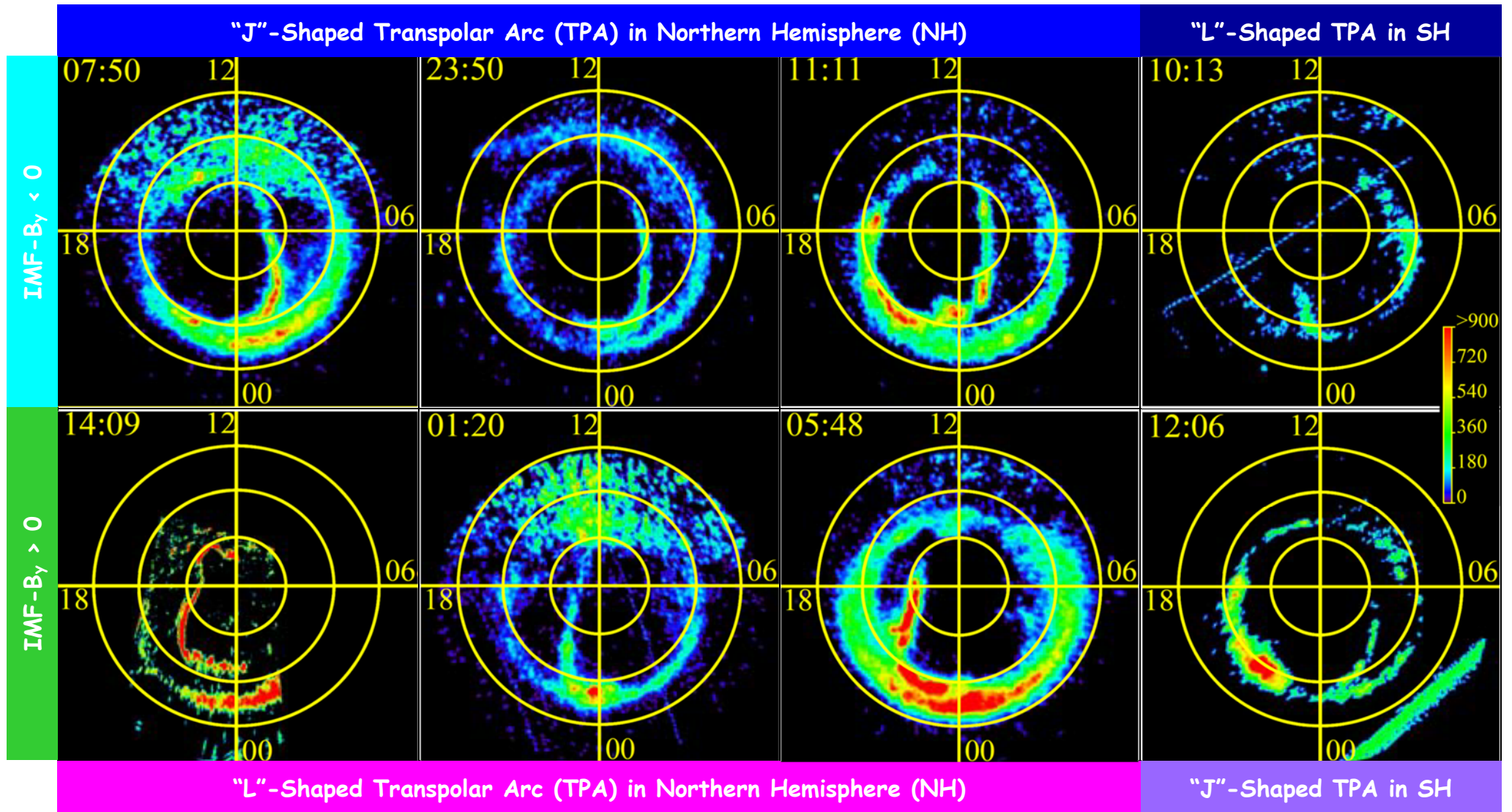


1046 Figure 7: A schematic illustration showing a possible scenario for the formation of nightside  
 1047 distorted TPAs in terms of the magnetic field configuration changes, field-aligned currents  
 1048 (FACs), the magnetic reconnection plasma flows and the reconnection point retreats is shown.  
 1049 This illustration includes the observational examples of the “L”-shaped TPA, obtained by the  
 1050 IMAGE FUV-WIC on November 5<sup>th</sup> 2000, the counter-clockwise current vortex in close  
 1051 proximity to the “L”-shaped TPA on March 12<sup>th</sup> 2002, induced by FACs flowing out of the  
 1052 ionosphere, and direct measurement of upward FACs across the “L”-shaped TPA on October  
 1053 28<sup>th</sup> 2003, detected by DMSF-F14. The magnetotail cross section and twisted plasma sheet are  
 1054 shown with a gray-shaded circle and red bar, respectively. FACs flowing toward magnetotail are  
 1055 indicated by orange curved arrows. Thin blue arrows show the fast plasma flows generated by  
 1056 magnetotail magnetic reconnection. The progressive retreat profile of the reconnection points  
 1057 (red dots) from  $T_0$  to  $T_3$  is shown with thick red arrows.

Figure 1.

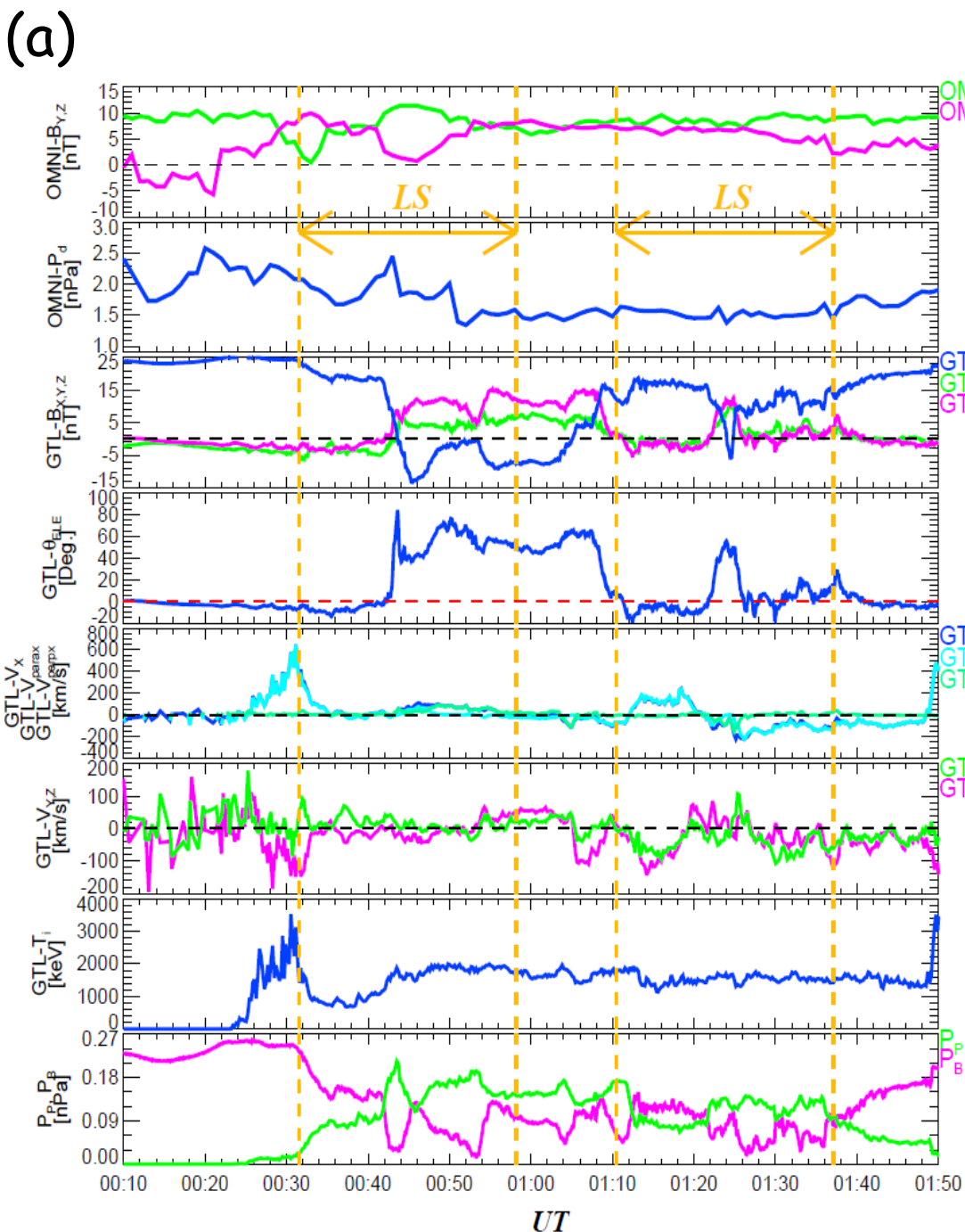


(a) 2000/9/22 7:50:26 UT (b) 2000/12/27 23:50:07 UT (c) 2001/12/31 11:11:49 UT (d) 2004/6/5 10:13:40 UT

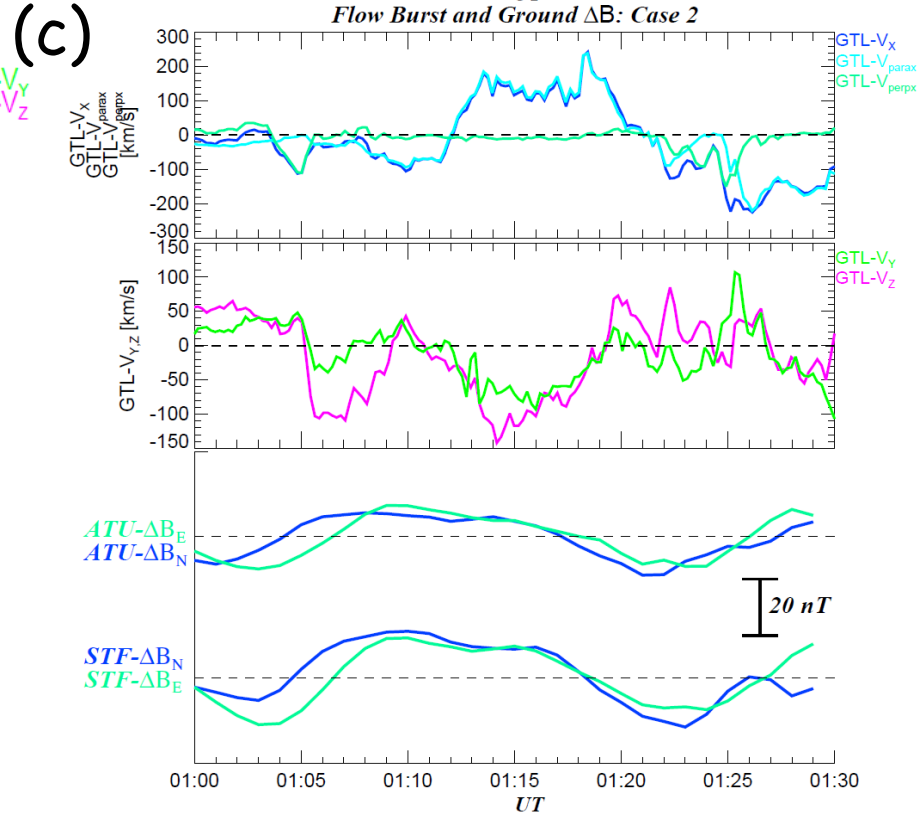
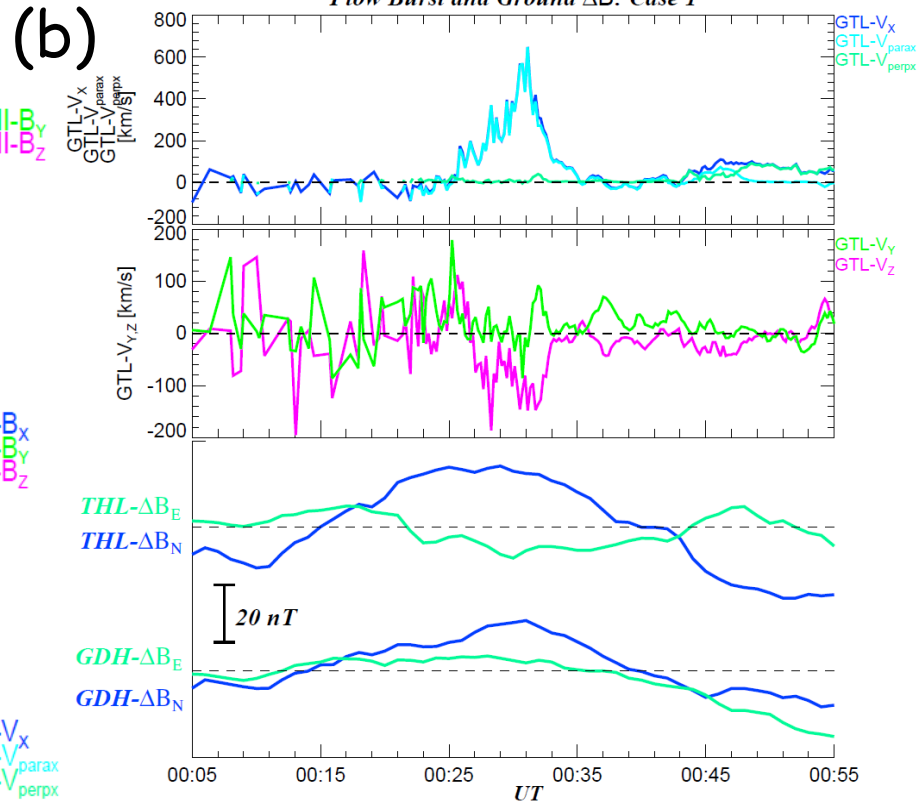


(e) 2003/10/28 14:09:42 UT (f) 2002/3/12 1:20:43 UT (g) 2000/11/5 5:48:42 UT (h) 2005/6/1 12:06:09 UT

Figure 2.



GTL Location during First "L"-Shaped TPA in GSM: (-25.54, 5.17, 6.02)  
 GTL Location during Second "L"-Shaped TPA in GSM: (-25.88, 4.92, 5.82)



(d)

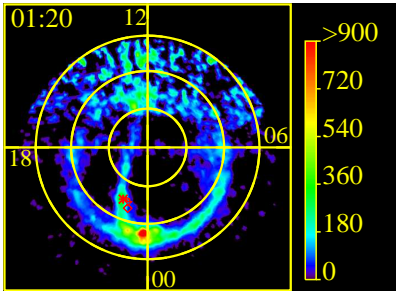
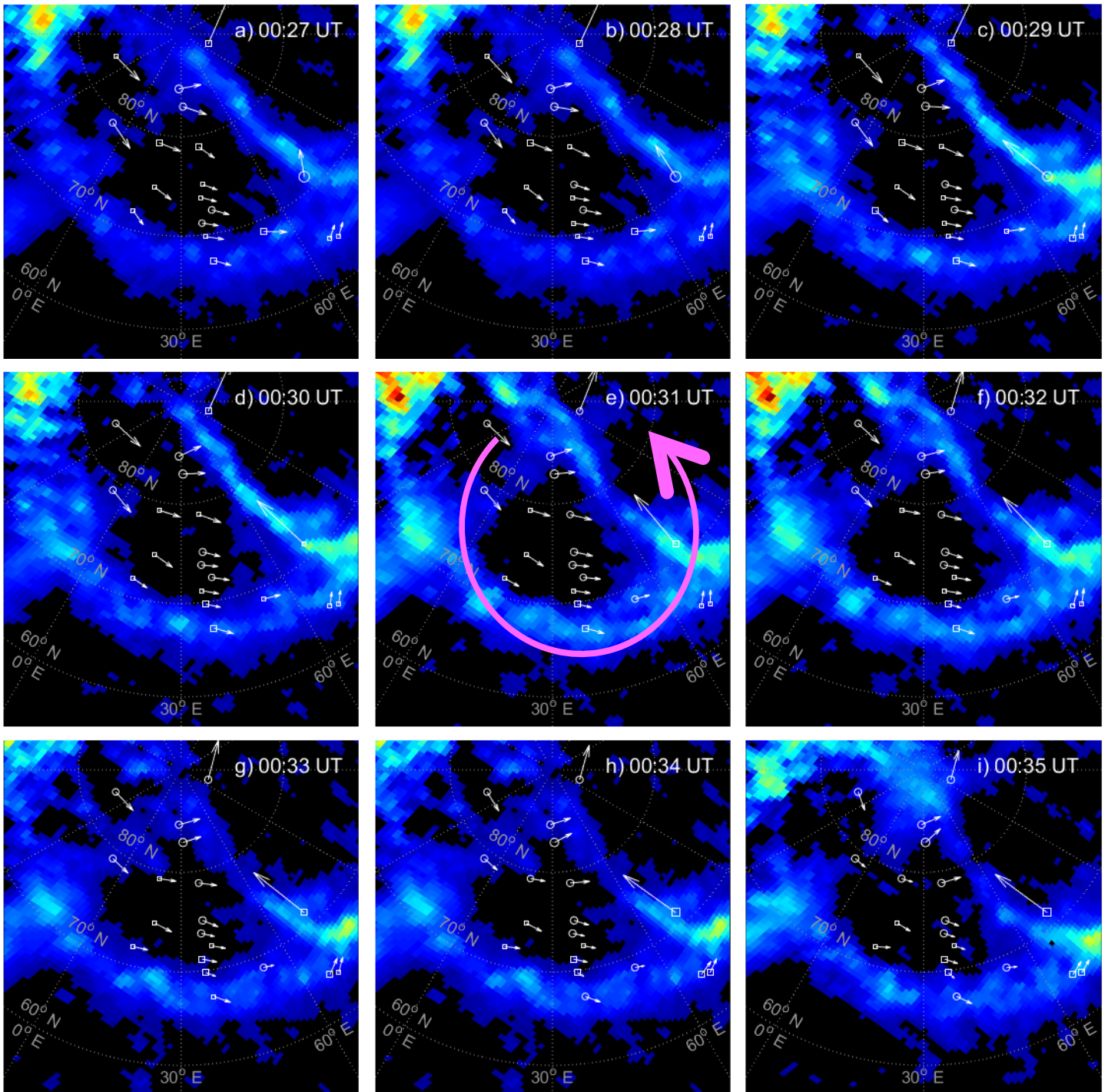


Figure 3.



(A)



(B)

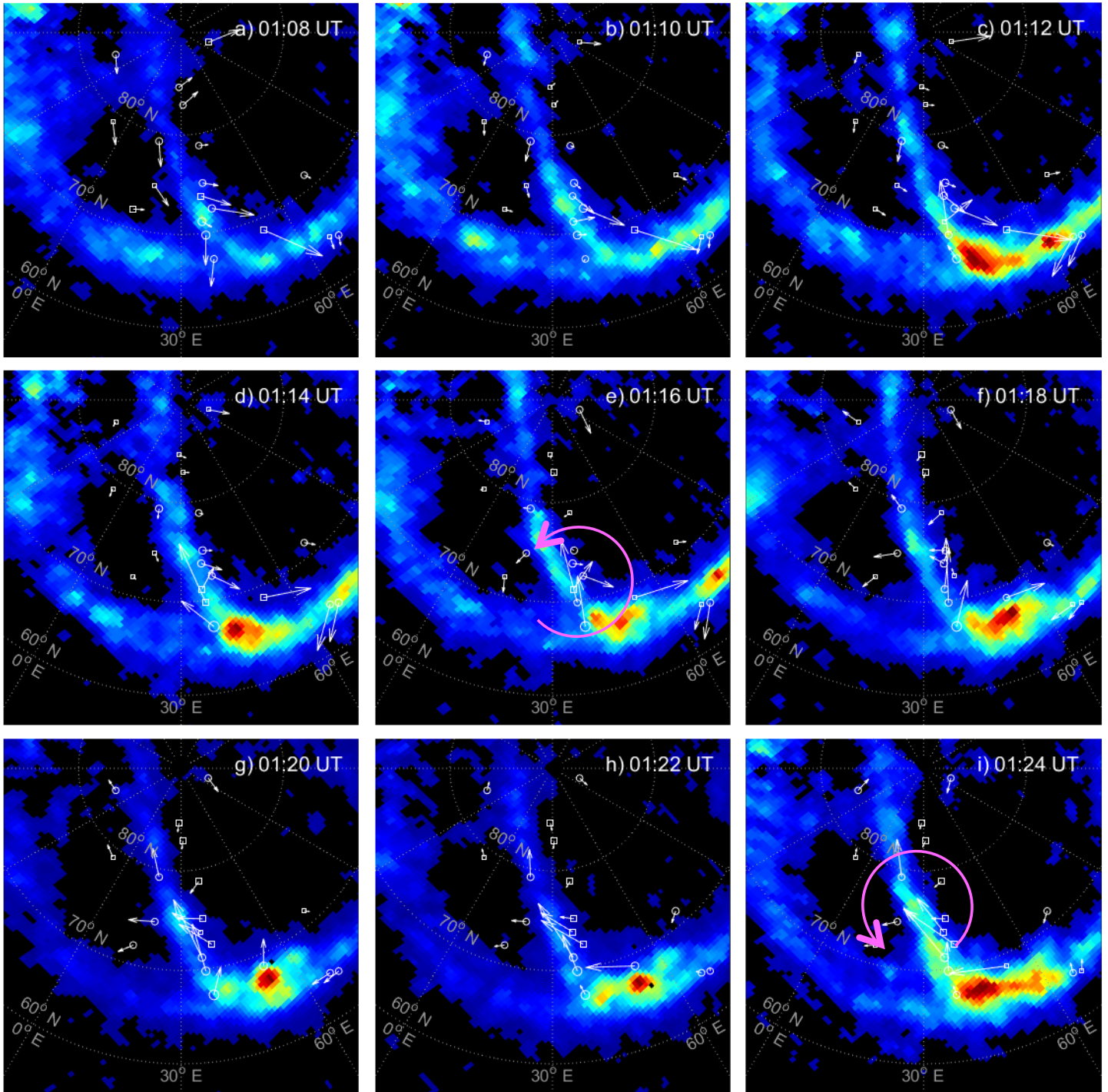
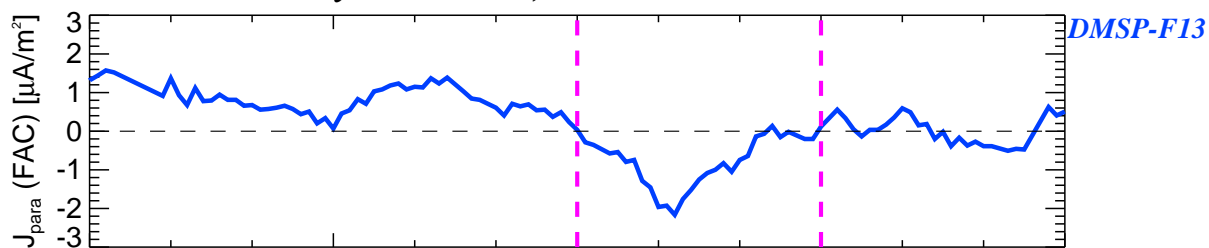


**Figure 4.**



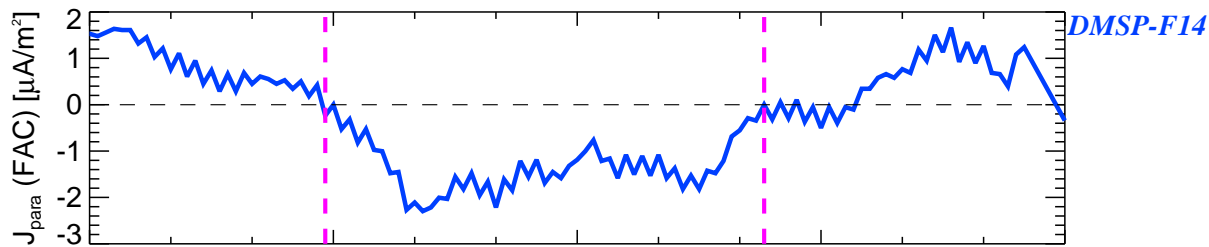
**FACs during the "L"-shaped TPA  
Observed by DMSP-F13,-F14 and -F16 on 2003/10/28**

(a)



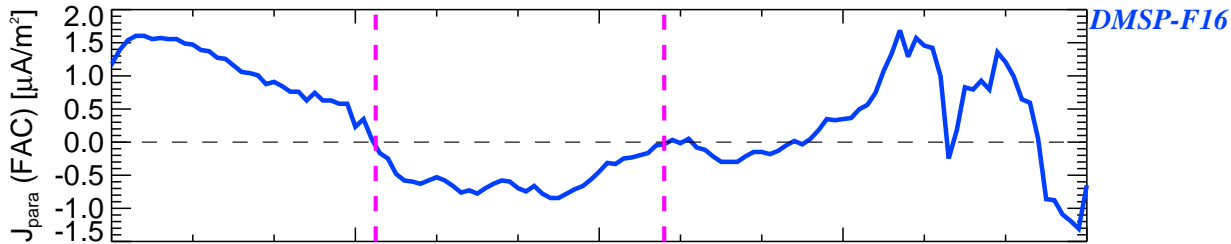
<i>UT</i>	13:44:00	13:44:30	13:45:00	13:45:30	13:46:00
<i>MLAT</i>	79.7800	81.1700	82.5300	83.3700	84.4800
<i>MLON</i>	107.950	102.010	95.3700	86.7600	75.2800
<i>MLT</i>	16.6203	16.2309	15.7885	15.1778	14.3636

(b)



<i>UT</i>	14:01:30	14:02:00	14:02:30	14:03:00	14:03:30
<i>MLAT</i>	80.8600	81.8400	82.3700	82.7600	82.7300
<i>MLON</i>	102.110	93.8600	82.1100	73.2900	60.2400
<i>MLT</i>	16.5114	15.9717	15.1567	14.5455	13.6281

(c)



<i>UT</i>	13:59:00	13:59:30	14:00:00	14:00:30	14:01:00
<i>MLAT</i>	80.8400	81.4200	81.9500	81.9100	81.8000
<i>MLON</i>	97.7800	87.7600	77.4000	65.3600	53.5800
<i>MLT</i>	16.1889	15.4930	14.7697	13.9275	13.1019

Figure 5.



<i>Event</i>	<i>Average Retreat Velocity [km/s]</i>
<i>2000/09/22</i>	<i>1.16</i>
<i>2000/11/05</i>	<i>7.30</i>
<i>2001/12/31</i>	<i>3.05</i>
<i>2002/03/02</i>	<i>1.42</i>
<i>2002/03/12</i>	<i>12.30</i>

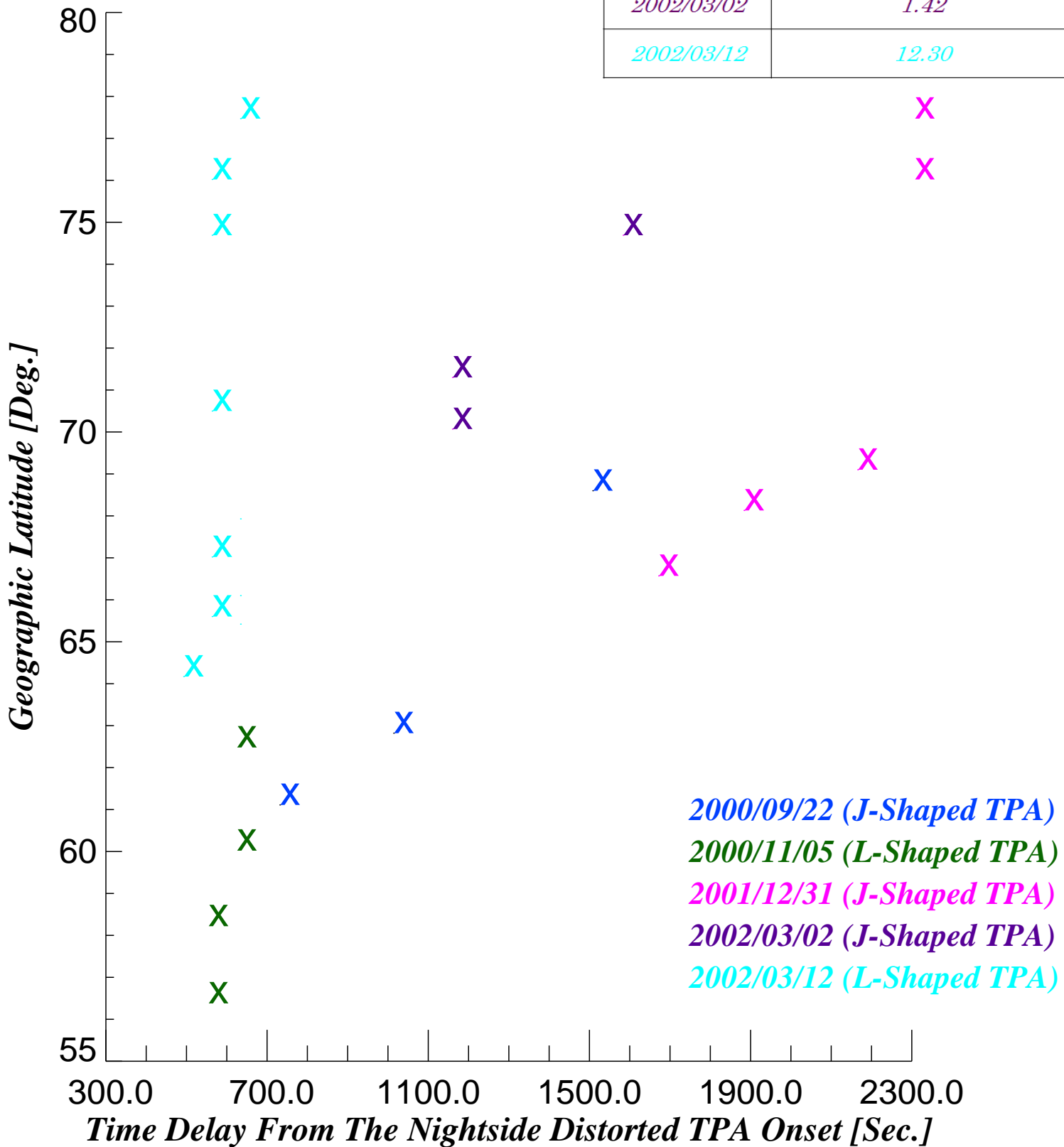
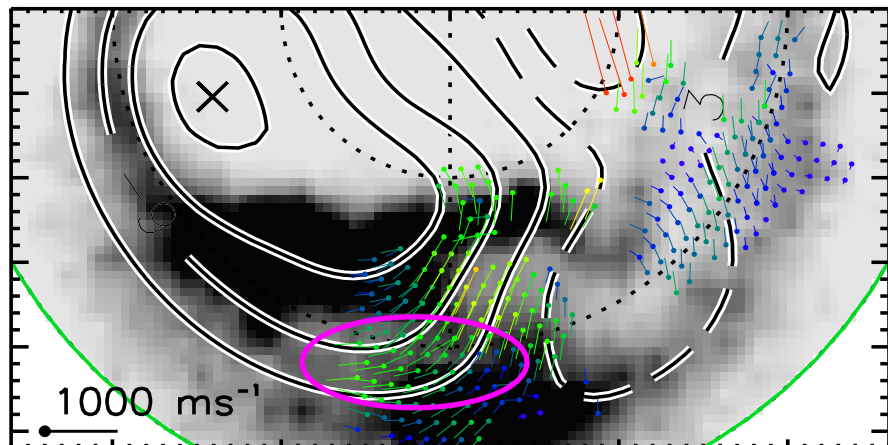
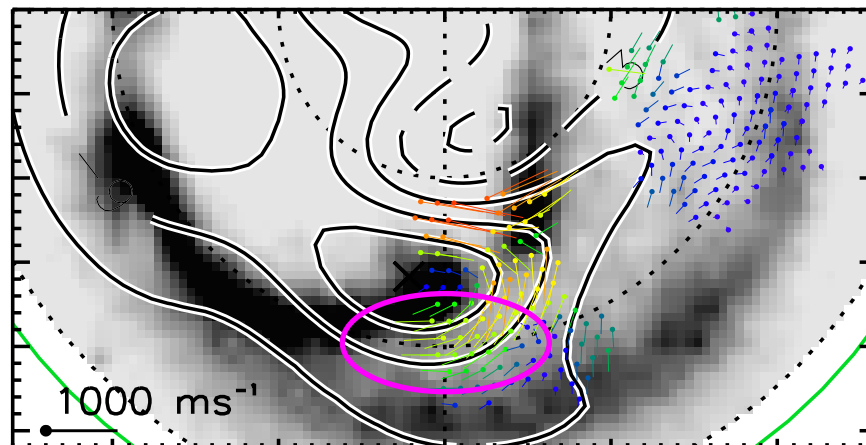


Figure 6.

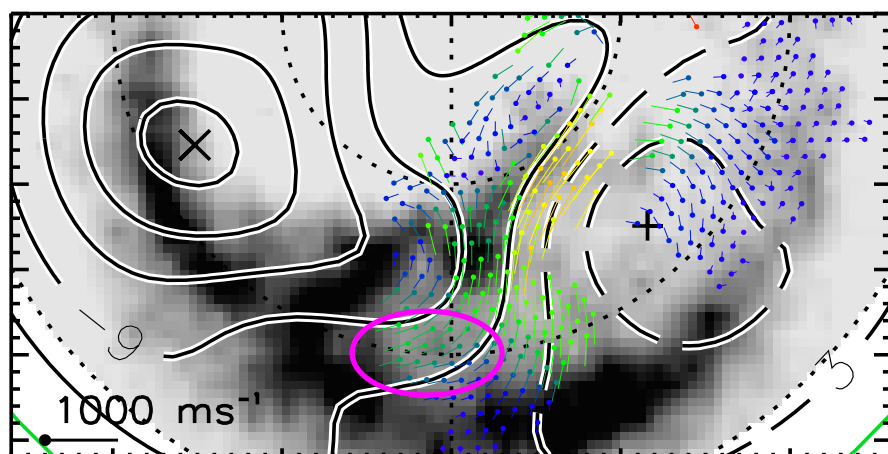
FUV time: 10:20:34 UT



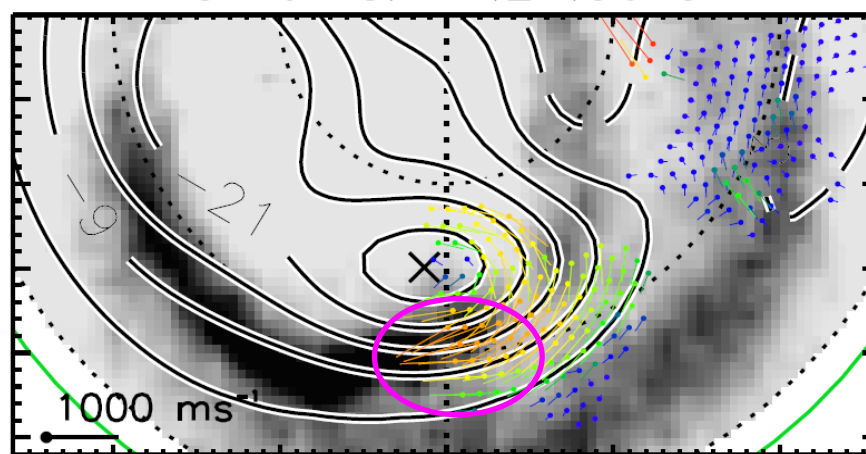
FUV time: 11:15:55 UT



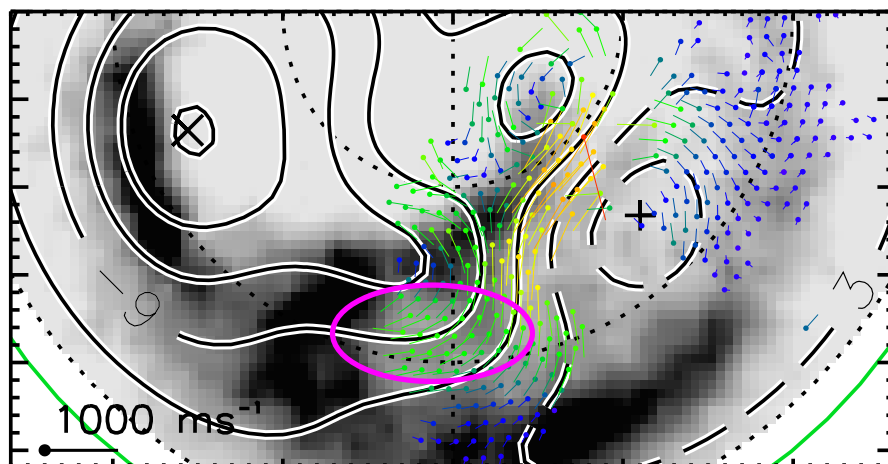
FUV time: 10:47:13 UT



FUV time: 11:24:06 UT



FUV time: 10:49:16 UT



FUV time: 11:28:13 UT

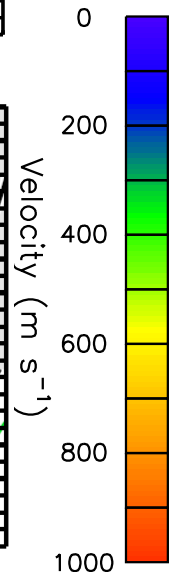
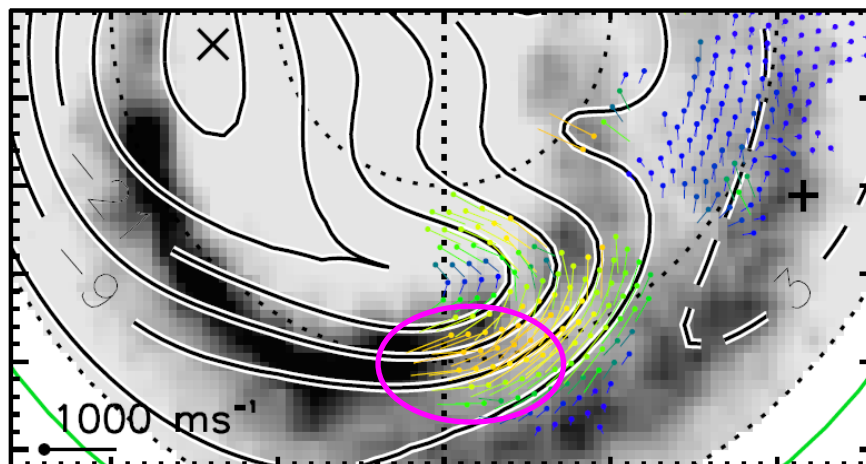
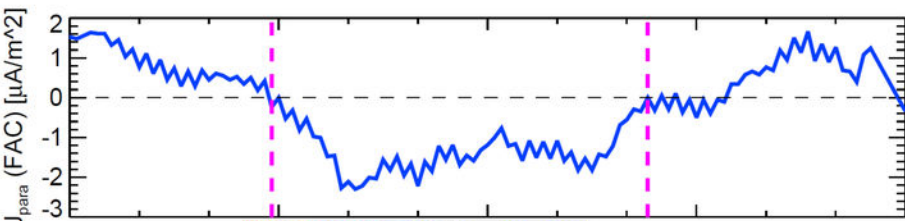


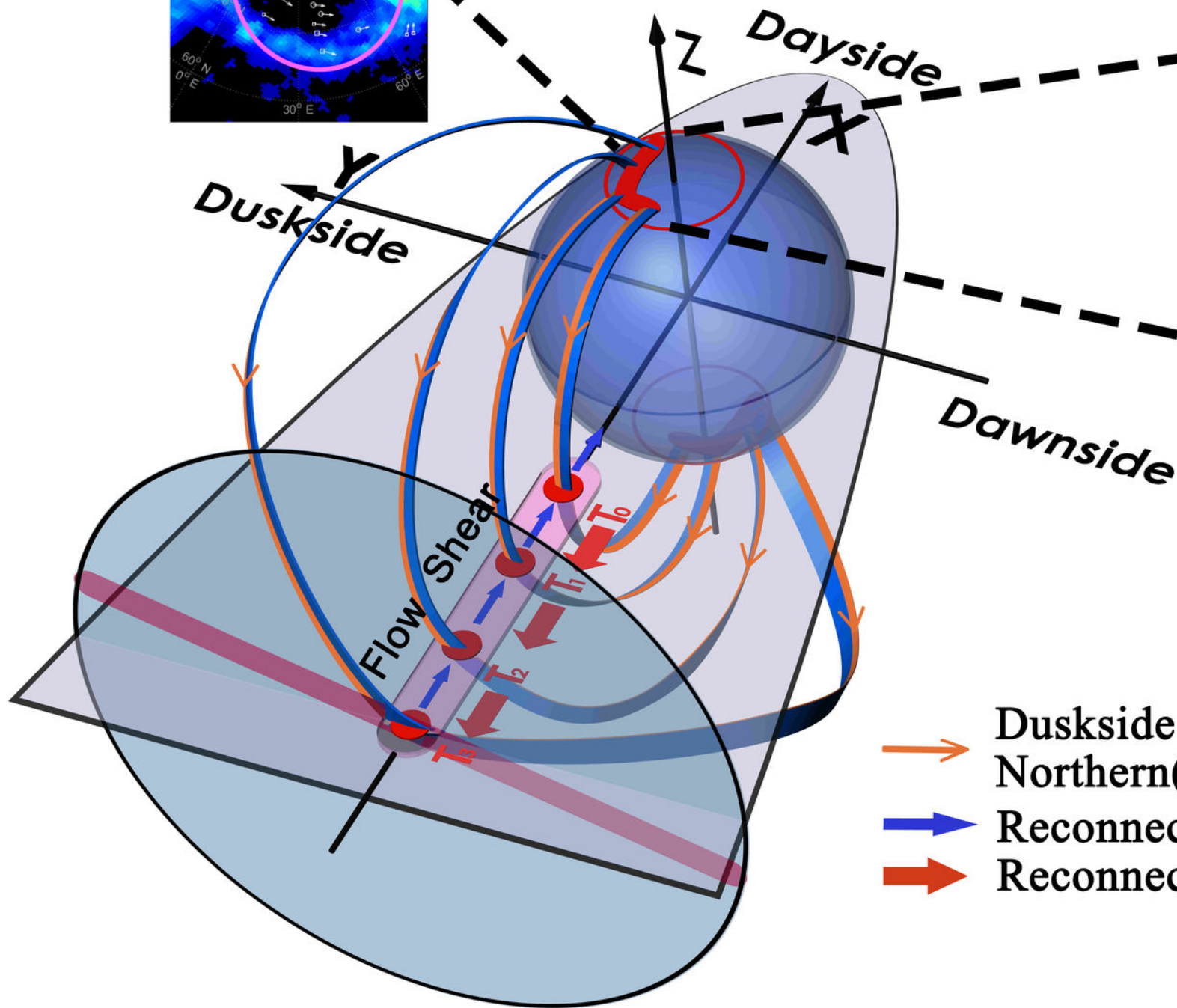
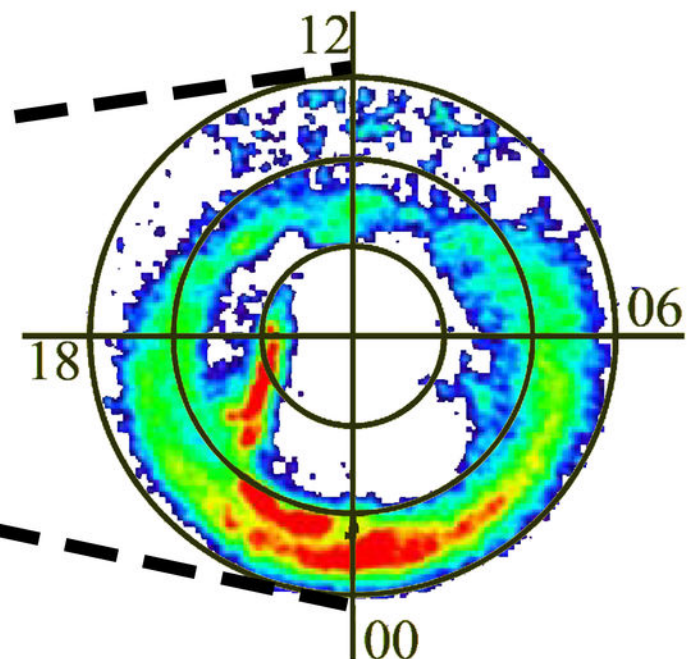
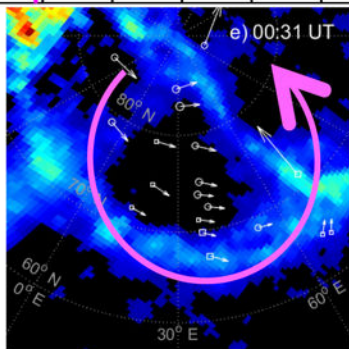
**Figure 7.**





# L-Aurora

## IMF-By > 0



- Duskside (Dawnside) Upward FACs in Northern(Southern) Hemisphere
- Reconnection flow
- Reconnective point Retreat